nature cardiovascular research

Article

https://doi.org/10.1038/s44161-024-00588-9

Cross-species comparison reveals that Hmga1 reduces H3K27me3 levels to promote cardiomyocyte proliferation and cardiac regeneration

Received: 15 December 2023

Accepted: 26 November 2024

Published online: 02 January 2025

Check for updates

Mara Bouwman[1,12], Dennis E. M. de Bakker[1,10,12], Hessel Honkoop[1], Alexandra E. Giovou[2], Danielle Versteeg[1], Arie R. Boender[2,3], Phong D. Nguyen[1,11], Merel Slotboom[1], Daniel Colquhoun[4], Marta Vigil-Garcia[1], Lieneke Kooijman[1], Rob Janssen[2], Ingeborg B. Hooijkaas[2], Marie Günthel[2], Kimberly J. Visser[1], Mischa Klerk[2], Lorena Zentilin[5], Mauro Giacca[5,6], Jan Kaslin[4], Gerard J. J. Boink[2,3,7], Eva van Rooij[1,8], Vincent M. Christoffels[2] & Jeroen Bakkers[1,9]

In contrast to adult mammalian hearts, the adult zebrafish heart efficiently replaces cardiomyocytes lost after injury. Here we reveal shared and species-specific injury response pathways and a correlation between Hmga1, an architectural non-histone protein, and regenerative capacity, as Hmga1 is required and sufficient to induce cardiomyocyte proliferation and required for heart regeneration. In addition, Hmga1 was shown to reactivate developmentally silenced genes, likely through modulation of H3K27me3 levels, poising them for a pro-regenerative gene program. Furthermore, AAV-mediated Hmga1 expression in injured adult mouse hearts led to controlled cardiomyocyte proliferation in the border zone and enhanced heart function, without cardiomegaly and adverse remodeling. Histone modification mapping in mouse border zone cardiomyocytes revealed a similar modulation of H3K27me3 marks, consistent with findings in zebrafish. Our study demonstrates that Hmga1 mediates chromatin remodeling and drives a regenerative program, positioning it as a promising therapeutic target to enhance cardiac regeneration after injury.

Myocardial infarction (MI) causes a massive loss of cardiomyocytes (CMs) that cannot be regenerated, an event that culminates in the formation of non-regenerative fibrotic scar tissue and a decline in heart function. The inability of the adult mammalian heart to regenerate is attributed to the very low CM turnover and cell-intrinsic properties, such as DNA content, and environmental conditions, such as oxygen levels, which collectively restrict the proliferative capacity of mammalian CMs[1–7]. Although the adult mammalian heart is unable to regenerate lost myocardium after injury, embryonic and neonatal hearts do possess regenerative capacity[8]. This observation suggests the presence of a latent cardiac regenerative program in mammals that is silenced shortly after birth.

Several approaches to induce CM proliferation in mammals, including inhibiting the Hippo pathway[9,10], activating erb-b2 receptor tyrosine kinase (ErbB2) signaling[11] and overexpressing microRNAs[12], have demonstrated promise in regenerating the injured heart. However,

A full list of affiliations appears at the end of the paper. e-mail: j.bakkers@hubrecht.eu

the widespread and injury-independent CM proliferation induced by these methods can also lead to detrimental outcomes, including cardiomegaly[11,13–15], reduced cardiac contractility[16] and arrhythmias[17]. This underscores the pressing need for spatiotemporal control over pro-regenerative stimuli to avert these adverse effects, thus enabling their therapeutic application[18].

In contrast to mammals, zebrafish regenerate an injured adult heart efficiently without adverse effects[19]. In the injured zebrafish heart, CMs within the injury vicinity, also known as the border zone (BZ), undergo a transformative process characterized by changes in chromatin organization, de-differentiation and proliferation, all of which facilitate the replacement of lost CMs[5,20–26]. Although a BZ also forms in the adult mouse heart after MI[27–30], the observed transcriptional changes fail to reactivate the cell cycle in CMs. The enigma of species-related differences in injury response remains a largely uncharted territory, with a paucity of knowledge about the molecular mechanisms underlying these variations.

Interspecies and intraspecies comparisons of transcriptional programs have proven very effective in uncovering mechanisms that drive tissue regeneration[31,32]. For instance, an interspecies transcriptome analysis between medaka fish, which lack efficient heart regeneration, and zebrafish revealed differences in the innate immune response after cardiac injury, highlighting the importance of the immune response during regeneration versus scarring[33]. Moreover, an intraspecies comparison in *Astyanax mexicanus* fish revealed that efficient heart regeneration in a surface population and its absence in a cave-dwelling population correlates well with the expression of *lrrc10* (leucine-rich repeat containing 10), a gene pivotal for cardiomyocyte redifferentiation and maturation[26,34]. In our study, we set out to unravel the shared and species-specific responses to injury within the BZ between mouse and zebrafish, aiming to reveal the mechanisms that drive natural heart regeneration. Our hypothesis posits that harnessing these natural responses in the mammalian heart will induce heart regeneration without detrimental effects, such as cardiomegaly or lethal arrhythmias.

Our study unveils substantial transcriptional shifts within the BZ of injured zebrafish and mouse hearts, marked by activation of a stress program, extracellular matrix remodeling and a simultaneous reduction in metabolic gene expression linked to mitochondrial oxidative phosphorylation. Notably, we identified high-mobility group AT-hook protein 1 (Hmga1), a conserved architectural chromatin protein, whose expression correlates with regenerative potential in zebrafish, neonatal mouse and neonatal human hearts. In zebrafish, Hmga1 is a prerequisite for the re-expression of embryonic genes, CM proliferation, scar resolution and the induction of a regenerative program. Hmga1a achieves this by clearing repressive histone 3 lysine 27 trimethylation (H3K27me3) marks from gene bodies of embryonic and metabolic genes, typically silenced in adult CMs but reactivated during regeneration. Notably, inducing Hmga1 expression in BZ CMs of injured mouse hearts triggers a regenerative program, fostering CM proliferation and functional recovery. Moreover, in mouse BZ CMs overexpressing Hmga1, we found a similar decrease in H3K27me3 repressive marks consistent with findings in zebrafish, indicating that Hmga1 has a conserved function. This insight into Hmga1-driven mechanisms that decrease these repressive histone marks introduces transformative potential for regenerative therapies in repairing injured hearts.

Results

Hmga1a is an essential regulator of zebrafish heart regeneration

The BZ in the injured zebrafish heart can be regarded as a local environment composed of various cell types (for example, immune cells, endothelial cells, cardiomyocytes and fibroblasts) that is permissive for CM proliferation. Although these cell types are also present in the BZ of injured mouse and human hearts, their presence and interactions do not lead to cell cycle re-entry of CMs[30,35]. To reveal the molecular differences among BZ microenvironments, we performed spatial transcriptomic analysis on injured zebrafish and mouse hearts. For the spatial transcriptomics, we used a method that we developed previously, called TOMO-seq[24,36], on injured zebrafish and mouse hearts at 3, 7 and 14 days post injury (dpi). Although, for zebrafish, the entire ventricle was processed, we used *BAC-Nppb-Katushka* mice to visualize the BZ after MI[37] and isolated a region of the heart including the injury area (IA), the BZ and the remote zone (RZ) for TOMO-seq (Fig. 1a). Pearson's correlation analysis across all genes for each pairwise combination of sections revealed clusters of genes with expression in the different areas (IA, BZ and RZ) (Fig. 1b). Based on these gene clusters as well as marker gene expression, we identified the locations of the IA (cluster 1, *Rhoc* (ras homolog family member C), *Fstl1* (follistatin-like 1) and *Tmsb4x* (thymosin beta 4)); the BZ (cluster 2, *Nppa* (natriuretic peptide type A), *Des* (desmin) and *Ankrd1* (ankyrin repeat domain 1)); and the RZ (cluster 3, *Tnnt2* (troponin T2), *Tnni3* (troponin I) and *Ech1* (enoyl coenzyme A hydratase 1)) within the TOMO-seq datasets, which were validated through in situ hybridization (ISH) (Fig. 1c).

To allow for an interspecies comparison, we identified all genes that were differentially expressed in the BZ compared to the IA and RZ for both the zebrafish and mouse datasets (Supplementary Tables 1 and 2) and pooled the different timepoints to mitigate any temporal differences between both species. We identified all differentially expressed BZ genes with an annotated homolog in the mouse and zebrafish genomes and plotted, for each of these gene pairs, the log fold change (logFC) (BZ versus the rest of the tissue) (Fig. 2a,b). This comparison of BZ transcriptomes combined with Gene Ontology (GO) analysis revealed that genes with a function in oxygen-dependent metabolism (OXPHOS) were downregulated in the BZ of both species, reflecting the metabolic reprogramming of BZ CMs[5,21,24,30,38] (Extended Data Fig. 1a–d and Supplementary Tables 3–6). In addition, genes with a role in extracellular matrix remodeling and calcium binding were upregulated in the BZ of both species. To validate the overlap between the transcriptomic profile of the zebrafish and mammalian BZ, we compared our TOMO-seq data with previously published transcriptomics datasets obtained from human hearts after MI[39]. This comparison identified a significant overlap between the published human BZ genes and the mouse and zebrafish BZ genes revealed by our TOMO-seq analysis. In total, we found 102 genes overlapping among the human, mouse and zebrafish BZ lists, including *NPPB*, *ANKRD1* and *DES* (Extended Data Fig. 1e), which were validated through ISH (Extended Data Fig. 1f).

To identify genes that may promote regeneration, we focussed on genes that are upregulated only in the zebrafish BZ, with no known upregulated mouse homolog (Extended Data Fig. 1c). The zebrafish-specific BZ profile was enriched in genes related to actin binding, myofibrils and heart development as well as genes related to regulation of proliferation and spindle formation, which is consistent with CM dedifferentiation and redifferentiation[22,26,40] and CM proliferation[5,41], respectively, in the BZ of the zebrafish heart. To identify potential drivers of cardiac regeneration from the list of 371 zebrafish-specific BZ genes, we focused on genes with a potential regulatory function, specifically transcription factors, chromatin-associated factors and genes with a known regulatory role in major signaling pathways. As a result, we selected 20 genes for further experimental investigation (Extended Data Fig. 2a–c and Supplementary Table 7). To enrich for genes with a potential cell-autonomous function in BZ CMs, we explored their spatial expression pattern in zebrafish using ISH. Of the 20 candidates, nine showed expression predominantly in BZ CMs, whereas 11 candidates showed expression mostly in non-CMs. Additionally, quantitative polymerase chain reaction (qPCR) analysis confirmed, for six of nine candidates, that their expression was not upregulated in the mouse BZ. Finally, three candidates were selected for functional follow-up experiments, which had not been implicated in cardiac regeneration. For the remaining three candidate genes, knockout zebrafish lines were produced: *khdrbs1a* (KH domain-containing, RNA-binding, signal

https://doi.org/10.1038/s44161-024-00588-9

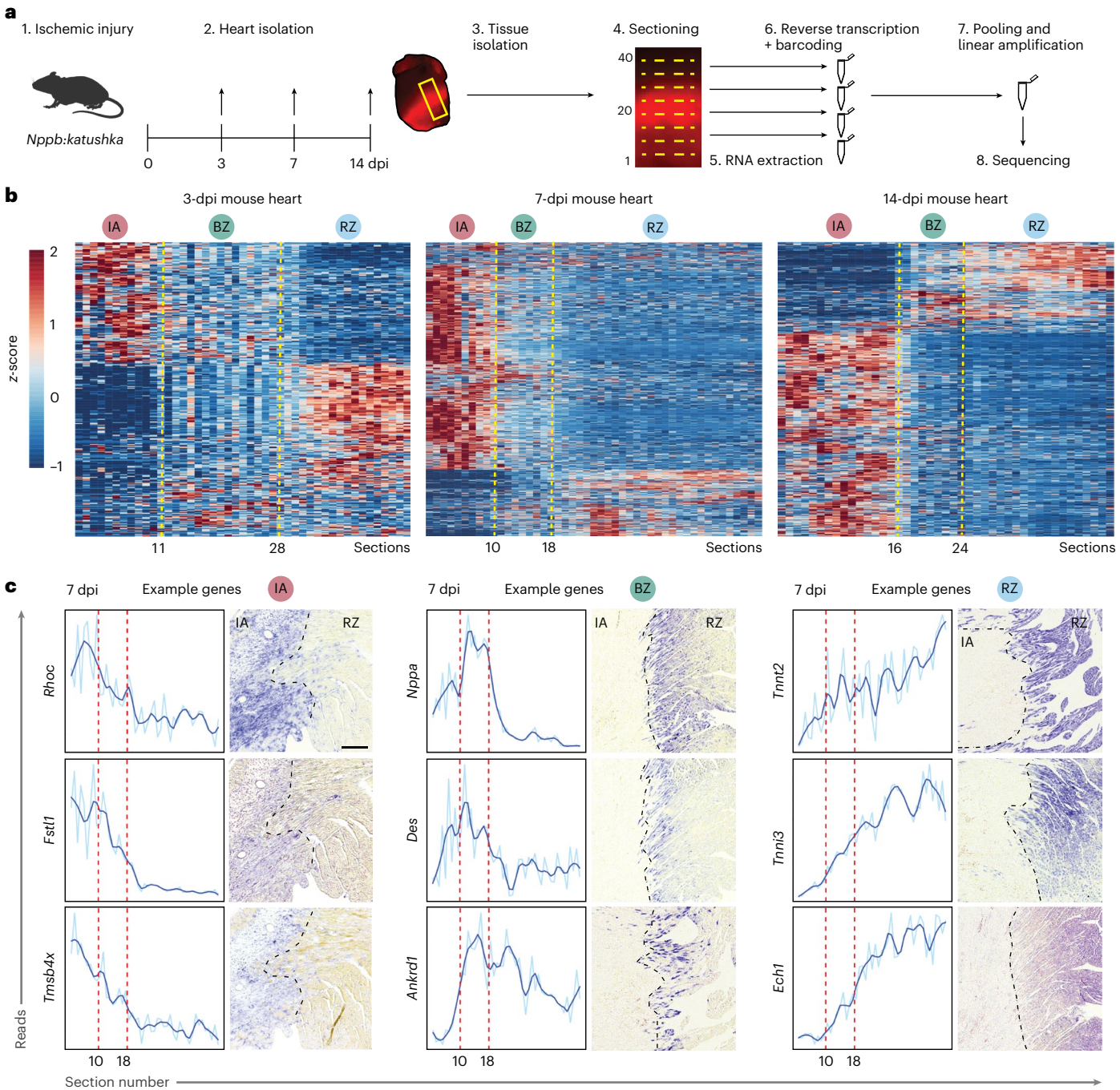

Fig. 1 | TOMO-seq reveals transcriptionally distinct regions in the injured mouse heart. a, Schematic overview of TOMO-seq workflow on injured mouse hearts. **b**, Three-dpi, 7-dpi and 14-dpi heatmaps showing hierarchical clustering for genes with a clear expression peak (*z*-score > 1 in more than four consecutive sections). Genes are on the *y* axis, and section numbers are on the *x* axis. Each section represents 100 µm of tissue. IA, BZ and RZ indicate consecutive sections with distinct gene profiles, separated by yellow dotted lines. **c**, Seven-dpi TOMO-seq plots with paired ISH images showing three representative genes for each zone. A total of $n = 3$ hearts were analyzed per staining. Red dashed lines in TOMO-seq plots indicate borders between IA, BZ and RZ, and black dashed lines in images indicate the border of the IA. Scale bar, 200 µm, which is the same for all ISH images.

transduction-associated 1a), *znfx1* (zinc finger NFX1-type containing 1) and *hmga1a* (high-mobility group AT-hook 1a). While *khdrbs1a* mutant fish displayed a lethal phenotype preventing the assessments of its role during heart regeneration, *znfx1* and *hmga1a* mutants were viable as adults. To investigate the potential functional role of Znfx1 and Hmga1a on zebrafish heart regeneration, we performed cryoinjuries on *znfx1* and *hmga1a* mutants and investigated CM proliferation in the BZ and scar regression. Although *znfx1* mutants showed no difference in CM proliferation and scar regression (Extended Data Fig. 2d,e), *hmga1a* mutants showed reduced BZ CM proliferation as well as impaired scar regression (Fig. 2c–f').

As the pipeline narrowed our focus on *hmga1a*, we sought to analyze expression in injured zebrafish, mouse and human hearts in more detail. We observed that *hmga1a* expression in both uninjured and 1-dpi zebrafish hearts was undetectable, whereas, at 3 dpi and 7 dpi, *hmga1a* expression was consistent in the BZ with robust *hmga1a* expression in BZ CMs at 7 dpi (Fig. 2g). As the zebrafish genome contains two *hmga1* genes (*hmga1a* and *hmga1b*), expression of both genes was analyzed,

https://doi.org/10.1038/s44161-024-00588-9

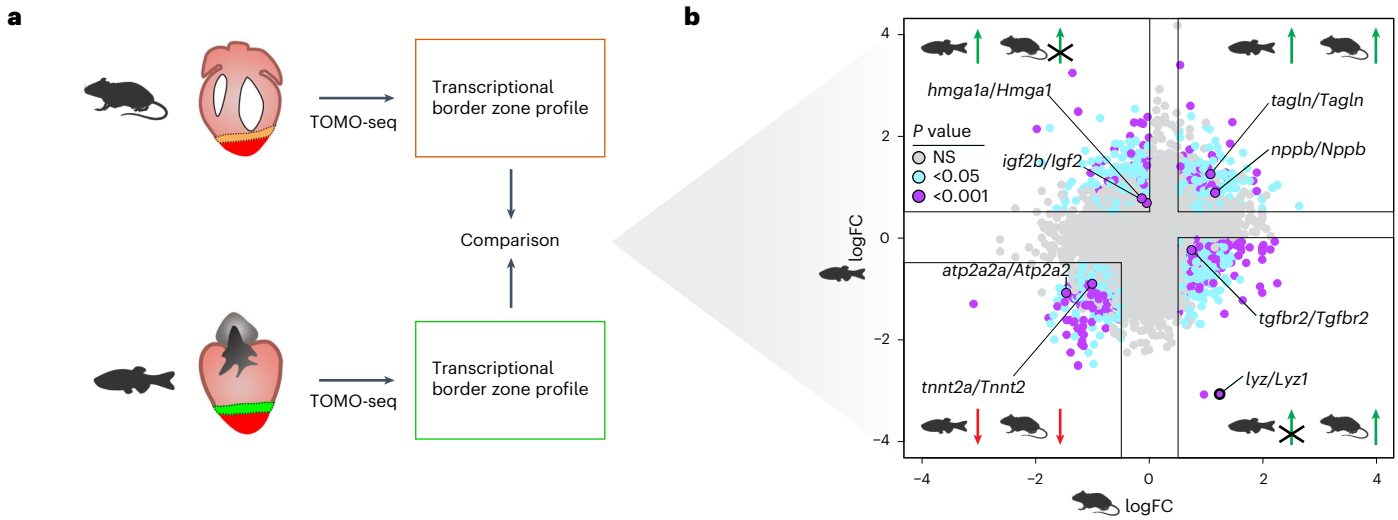

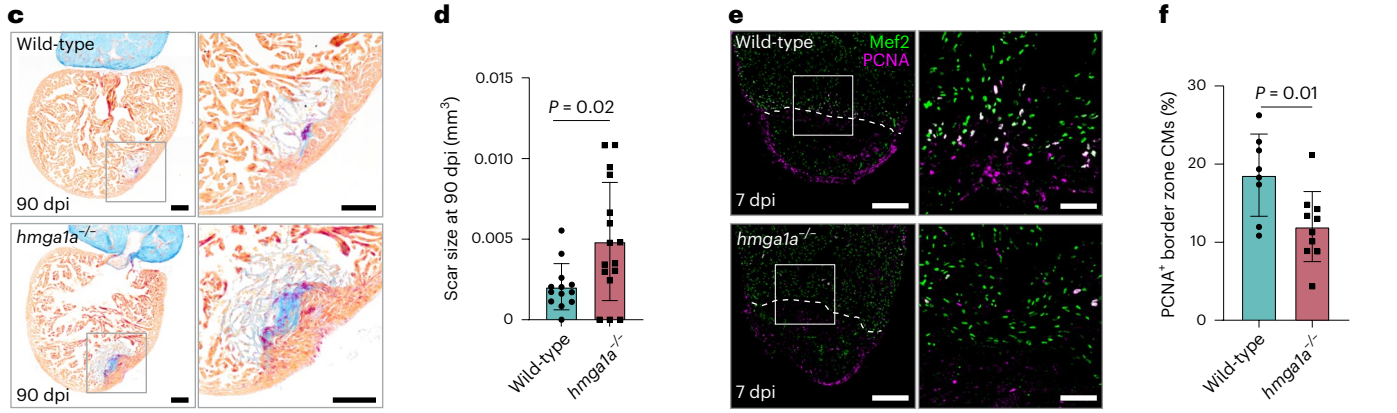

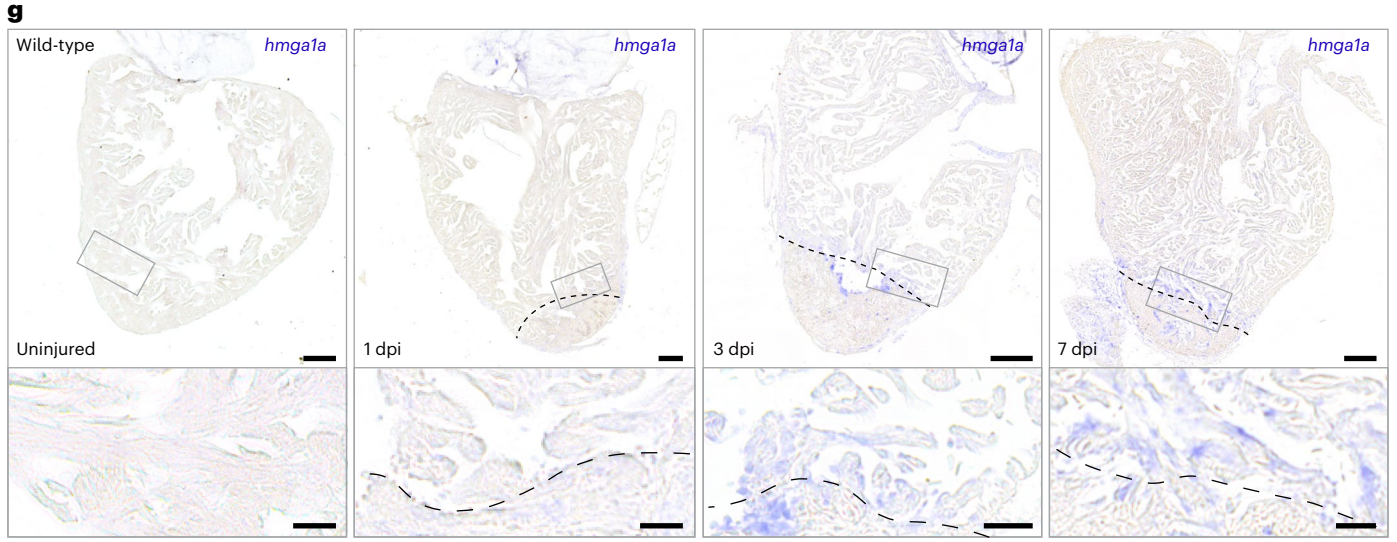

Fig. 2 | Interspecies comparison identifies Hmga1a, which spatially and temporally correlates with cardiac regenerative capacity. a, Schematic overview of the spatially resolved transcriptomic comparison of injured zebrafish and mouse BZs. **b**, Scatterplot analysis comparing BZ expression as logFC for homologous gene pairs. Gene pairs were selected based on the following criteria: only up in zebrafish (upper left quadrant); zebrafish logFC > 0.5, $P < 0.05$, and mouse logFC < 0; up in zebrafish and mouse (upper right quadrant); zebrafish logFC > 0.5, $P < 0.05$, and mouse logFC > 0.5, $P < 0.05$; down in zebrafish and mouse (lower left quadrant); zebrafish logFC < −0.5, $P < 0.05$, and mouse logFC < −0.5, $P < 0.05$; and only up in mouse (lower right quadrant); zebrafish logFC < 0 and mouse: logFC > 0.5, $P < 0.05$. Statistics were obtained using the R package edgeR, which uses GLMs and empirical Bayes methods to identify differentially expressed genes. NS, not significant. **c**, Representative images of AFOG staining on 90-dpi wild-type and *hmga1a*$^{-/-}$ zebrafish hearts, showing muscle in orange, fibrin in red and collagen in blue. Scale bars, 100 µm. **d**, Quantification of scar size in wild-type ($n = 13$) and *hmga1a*$^{-/-}$ ($n = 16$) hearts at 90 dpi. Datapoints represent individual hearts. Error bars indicate mean ± s.d. Statistics were performed by two-tailed unpaired *t*-test ($P = 0.02$). **e**, Representative images of immunofluorescent staining against Mef2 and PCNA on 7-dpi wild-type and *hmga1a*$^{-/-}$ zebrafish hearts. Dashed line indicates border with the injury. Overview scale bars, 100 µm; zoom-in scale bars, 20 µm. **f**, Quantification of proliferating BZ CMs in wild-type ($n = 8$) and *hmga1a*$^{-/-}$ ($n = 10$) hearts at 7 dpi. Datapoints represent individual hearts. Error bars indicate mean ± s.d. Statistics were performed by two-tailed unpaired *t*-test ($P = 0.01$). **g**, Representative images of ISH against *hmga1a* in uninjured, 1-dpi, 3-dpi and 7-dpi zebrafish hearts. $n = 3$ hearts were analyzed per condition. Scale bars, 100 µm in overviews and 25 µm in zoom-ins. Dashed line indicates border with the injury.

https://doi.org/10.1038/s44161-024-00588-9

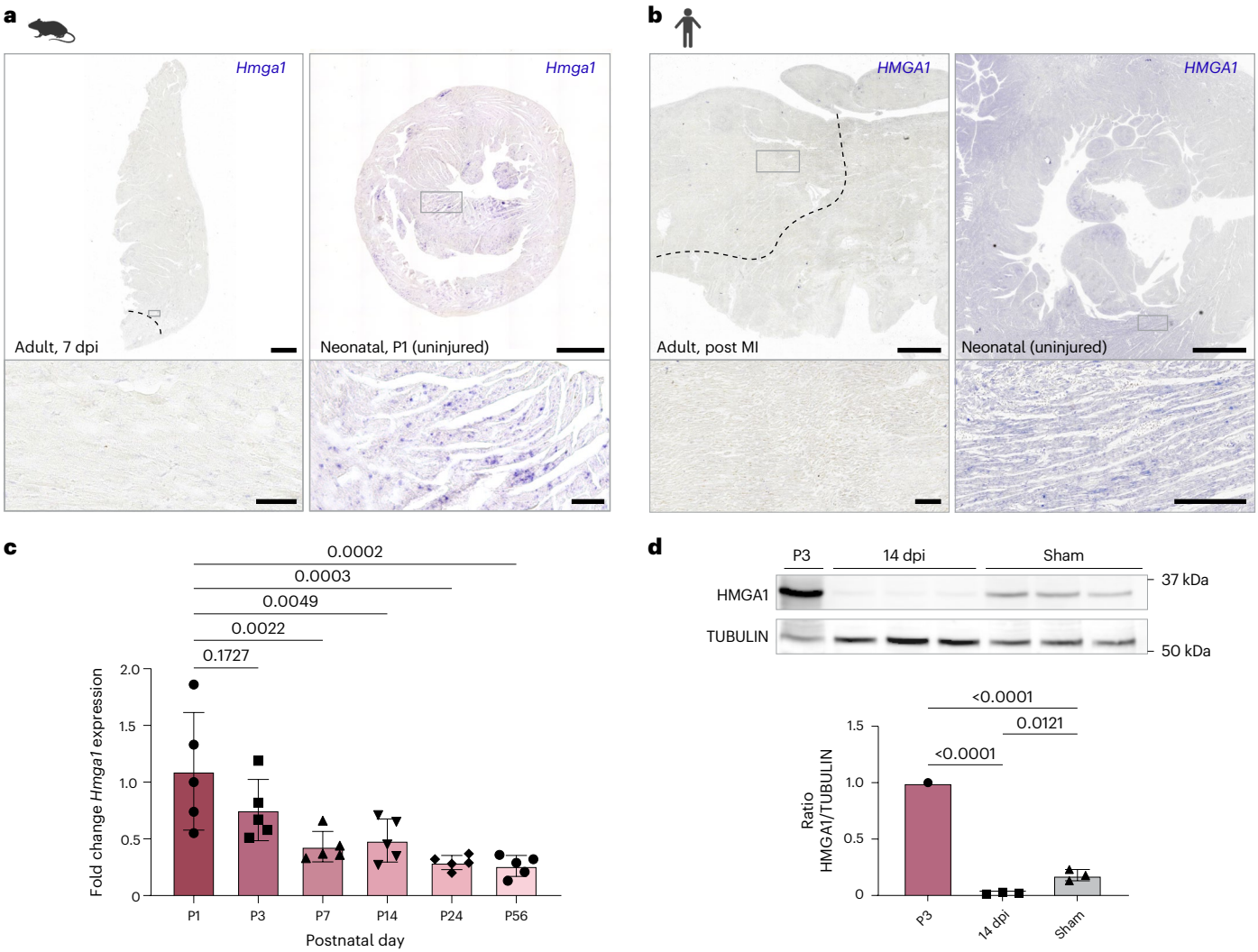

Fig. 3 | *Hmga1* correlates with regenerative capacity of the mammalian heart. **a**, Representative ISH for *Hmga1* in left ventricular tissue of injured adult mouse hearts (left panel) and in uninjured neonatal P1 mouse hearts (right panel). $n = 3$ hearts were analyzed per condition. Scale bars, 0.5 mm in the overview and 50 µm in the zoom-ins. Dashed line in the left panel indicates the injury border. **b**, Representative ISH images of *HMGA1* expression in intraventricular septum tissue of an injured adult human heart (left panel) and in an uninjured neonatal human heart (right panel). $n = 1$ heart was analyzed per condition. Scale bars, 3 mm in the overview and 250 µm in the zoom-ins. Dashed line in the left panel indicates the infarct border. **c**, qPCR results for *Hmga1* on cDNA libraries from whole mouse hearts at different postnatal timepoints. GAPDH was used as a reference gene. Five biological replicates were used per timepoint. Datapoints represent individual biological replicates. Error bars indicate mean ± s.d. Statistics were performed using a one-way ANOVA followed by Dunnett's multiple comparison test. One-way ANOVA analysis indicates a significant difference in *Hmga1* expression between different timepoints ($P = 0.0002$). Dunnett's multiple comparison test shows that P7 ($P = 0.0022$), P14 ($P = 0.0049$), P24 ($P = 0.0003$) and P56 ($P = 0.002$) significantly differ from the P1 timepoint, whereas P3 does not ($P = 0.1727$). **d**, Western blot for HMGA1 on protein lysate from 14-dpi ventricles ($n = 3$) and sham ventricles ($n = 3$) compared to a P3 ventricle ($n = 1$). TUBULIN was used as a control protein. Ratios were calculated using TUBULIN. Error bars indicate mean ± s.d. Statistics were performed using a one-way ANOVA followed by Tukey's multiple comparisons test and show that both 14-dpi samples ($P < 0.0001$) and sham samples ($P < 0.001$) significantly differ from the P3 sample. Fourteen-dpi samples and sham samples do not significantly differ from each other ($P = 0.021$).

revealing that *hmga1a* but not *hmga1b* expression is induced in BZ CMs upon injury (Extended Data Fig. 2f–h). In addition, *hmga1b* expression was not detectable in the *hmga1a* mutant hearts, suggesting that *hmga1b* does not compensate for the loss of *hmga1a* (Extended Data Fig. 2i). Notably, *Hmga1/HMGA1* expression was undetectable by ISH in injured adult mouse and human hearts (Fig. 3a,b). Reanalyzing previously published spatial transcriptomics data of human heart after MI[39] confirmed this absence of *HMGA1* expression (Supplementary Fig. 1). Contrary to adult hearts, ISH on mouse and human neonatal hearts showed abundant expression of *Hmga1/HMGA1* (Fig. 3a,b). Additionally, qPCR analysis demonstrated that *Hmga1* is expressed in neonatal mouse hearts at 1 day after birth (P1) and that its expression declines rapidly in the first week after birth, coinciding with the loss of regenerative capacity[8] (Fig. 3c). HMGA1 protein levels were confirmed to follow this pattern, with high protein abundance in a P3 mouse heart and significantly lower abundance in 14 dpi as well as sham hearts (Fig. 3d).

From these results, we conclude that *hmga1a/Hmga1/HMGA1* expression spatially and temporally correlates with the regenerative capacity of the zebrafish and mammalian heart and that *hmga1a* is required to stimulate efficient CM proliferation and heart regeneration in zebrafish.

BZ gene expression program is regulated by Hmga1a

Hmga proteins (Hmga1/Hmga2) are architectural chromatin proteins that contain three AT-hooks, enabling them to bind to the minor groove

https://doi.org/10.1038/s44161-024-00588-9

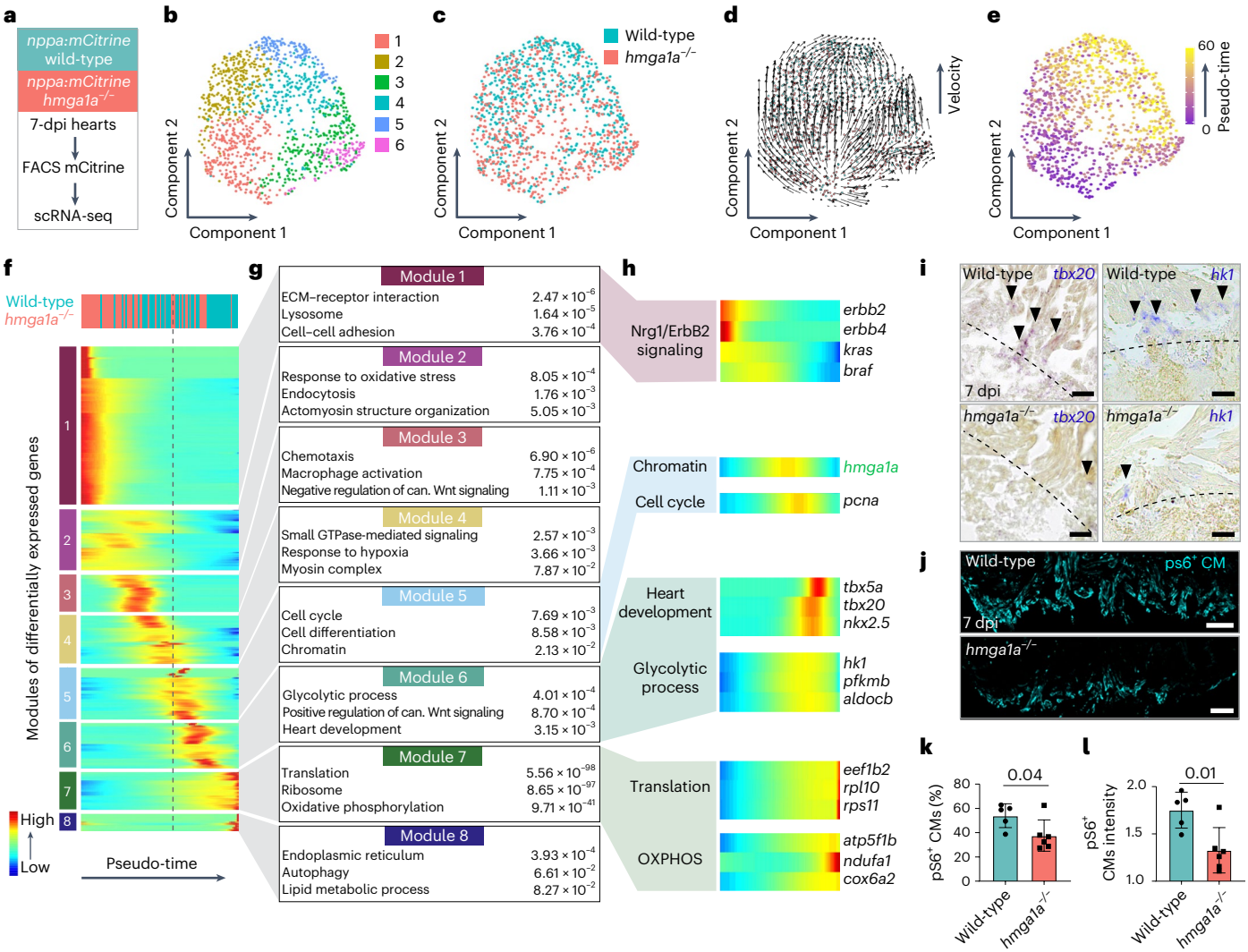

Fig. 4 | Hmga1a regulates progression of the regeneration program in BZ CMs. **a**, scRNA-seq workflow on *nppa:mCitrine*$^{+}$ cells from 7-dpi wild-type ($n = 12$) and *hmga1a*$^{-/-}$ ($n = 12$) hearts. **b**, UMAP representation of scRNA-seq data after unsupervised clustering by Seurat. **c**, Distribution of wild-type and *hmga1a*$^{-/-}$ cells over UMAP. **d**, RNA velocity plotted on UMAP. Arrows are vectors that indicate the present and future position of a cell in the UMAP based on the ratio of spliced and unspliced reads. **e**, Pseudo-temporal ordering of cells performed using Monocle 2 represented on UMAP. Scale from 0 to 60 (purple-yellow). **f**, Self-organizing heatmap of gene modules co-expressed over pseudo-time. Each line represents a single gene. Cells ordered based on pseudo-time are divided in 100 bins. Legend on the top shows the predominant genotype present in each bin. Dashed line indicates the beginning of module 5, containing *hmga1a*. **g**, Three representative GO terms and their *P* value (obtained using DAVID online GO analysis tool) are shown for genes in modules 1–8 of **f**. can., canonical. **h**, Heatmaps over pseudo-time of individual genes of interest from modules 1, 5, 6 and 7. Linked biological processes are indicated on the left of the heatmaps; gene names are indicated on the right. **i**, Representative images from ISH against *tbx20* (left) and *hk1* (right) showing part of the BZ of wild-type and *hmga1a*$^{-/-}$ hearts at 7 dpi. $n = 3$ hearts were analyzed per condition. Dashed line indicates the injury border. Arrowheads indicate *tbx20*/*hk1*-expressing CMs. Scale bars, 50 µm. **j**, Representative images from immunofluorescent staining showing myocardial pS6 in the BZ of wild-type and *hmga1a*$^{-/-}$ zebrafish hearts at 7 dpi. Scale bars, 100 µm. **k**,**l**, Quantification of myocardial pS6 signal in wild-type ($n = 5$) versus *hmga1a*$^{-/-}$ ($n = 6$) 7-dpi BZ. Datapoints represent individual hearts. Error bars indicate mean ± s.d. Statistics were performed by two-tailed unpaired *t*-test and show a significant difference in percentage of pS6^{+} area relative to tropomyosin^{+} area (**k**) ($P = 0.04$) and in intensity of pS6 signal relative to tropomyosin signal (**l**) ($P = 0.01$).

of AT-rich DNA[42]. By doing so, Hmga proteins can compete with histone H1, which is a linker histone that compacts chromatin, leading to more open and accessible chromatin and increased expression of undifferentiated and stem-cell-related genes[43–48]. To gain insight into the function of Hmga1a in the BZ, we performed single-cell RNA sequencing (scRNA-seq) on sorted BZ CMs using *Tg(nppa:mCitrine)* of both wild-type and *hmga1a* mutants at 7 dpi (Fig. 4a). We used uniform manifold approximation and projection (UMAP) to visualize expression of the pan-cardiomyocyte marker *myl7* (myosin light chain 7), which was uniformly high across all cells (Extended Data Fig. 3a). Additionally, the expression of BZ markers *nppa* and *desma* was widespread (Extended Data Fig. 3b,c), confirming that these cells are indeed BZ CMs. Unsupervised Seurat analysis on the scRNA-seq data identified six transcriptionally distinct cell clusters, indicating that BZ CMs adopt different cell states. Notably, *hmga1a* mutant and wild-type BZ CMs were unequally distributed across these clusters (Fig. 4b,c and Extended Data Fig. 3d,e), indicating that Hmga1a influences the transition into these different cell states. To further investigate this, we applied RNA velocity, which estimates the future transcriptional state of cells by modeling transcriptional dynamics[49], to our data. The model predicts whether the abundance of spliced mRNA will increase or decrease in the future, providing direction and magnitude for transcriptional changes. The resulting velocity vectors indicate the direction of predicted transcriptional shifts (Fig. 4d). We also performed pseudo-temporal ordering of

the cells using Monocle, which corroborated the RNA velocity findings (Fig. 4e). Both RNA velocity and pseudo-temporal ordering revealed a directional trend from the bottom of the UMAP plot toward the top, aligning with the distribution of *hmga1a* mutant cells (enriched at the bottom) and wild-type cells (enriched at the top). Based on these results, we conclude that (1) BZ CMs undergo transcriptional changes and (2) these changes are dependent on the presence of Hmga1a.

Next, we used the pseudo-temporal ordering to identify processes that occur in BZ CMs during regeneration, in which order they occur and how they depend on the presence of Hmga1a. Differential expression analysis of genes over pseudo-time and unsupervised clustering led to the identification of eight gene modules that consist of co-expressed genes (Fig. 4f and Supplementary Table 8). Modules 1–4 consisted of genes mainly involved in cell–cell interactions, immune response, stress and hypoxia (Fig. 4g). Pseudo-time modules 5–8 were enriched for genes with a role in cell cycle regulation, chromatin organization, heart development, energy metabolism and protein translation (Fig. 4g,h). Increased rates of translation[50] and oxidative phosphorylation[51] are correlated to cell cycle progression toward mitosis, and the reduced CM proliferation observed in *hmga1a* mutant BZ CMs may explain their observed downregulation. *hmga1a* was found in module 5, indicating that genes in modules 1–4 could potentially act upstream of Hmga1a. Corroborating such an upstream function, we observed that module 1 contained genes related to neuregulin (Nrg1)/ErbB2 signaling, which induces CM proliferation when activated[52] (Fig. 4g,h). Indeed, pharmacological inhibition of the Nrg1/ErbB2 pathway with the ErbB2 inhibitor AG1478 resulted in a significant reduction in *hmga1a* expression in BZ CMs (Extended Data Fig. 4a,b). In addition, intraperitoneal injection of recombinant NRG1 protein into uninjured zebrafish resulted in ectopic *hmga1a* expression throughout the entire heart (Extended Data Fig. 4c,d) and enhanced CM proliferation (Extended Data Fig. 4e). Finally, we also observed that NRG1-induced CM proliferation is largely dependent on Hmga1a activity, as NRG1 injection in *hmga1a* mutant hearts had no effect on CM proliferation compared to NRG1 injection in wild-type fish (Extended Data Fig. 4e). Of interest in modules 5–8 was the presence of *tbx5a* (T-box transcription factor 5a), *tbx20* (T-box transcription factor 20) and *nkx2.5* (NK2 homeobox 5), encoding cardiac transcription factors that are induced by injury[40], as well as *hk1* (hexokinase 1), encoding a rate-limiting enzyme for glycolysis, which is essential for BZ CM proliferation[5,41]. We confirmed reduced *hk1* and *tbx20* expression and reduced levels of phosphorylated ribosomal protein S6 (pS6, Ser253/263), a marker for translation rate[53], in *hmga1a* mutant BZ CMs, corroborating that genes in modules 5–8 are regulated by Hmga1a (Fig. 4i–l). Interestingly, mouse BZ CM gene expression determined by Calgagno et al.[54] showed a strong overlap with modules 1–4 (22%) but much less so with modules 5–8 (11%) (Supplementary Fig. 2), which is in good accordance with a lack of *Hmga1* expression and the low proliferative capacity of mouse BZ CMs.

Together, these results indicate that Hmga1a acts downstream of Nrg1/ErbB2 signaling to regulate the expression of cardiac transcription factors, cell cycle regulators and genes that regulate the metabolic reprogramming of BZ CMs during heart regeneration.

Hmga1a promotes cell cycle re-entry of CMs

As we observed that Hmga1a is required for cryoinjury-induced expression of embryonic cardiac genes and CM proliferation, we wanted to address whether *hmga1a* expression is sufficient to induce a regenerative program. Therefore, we generated a zebrafish line with tamoxifen-inducible and CM-specific *hmga1a* overexpression (OE), *Tg(ubi:Loxp-BFP-stop-Loxp-hmga1a-eGFP, myl7:CreERT2)*, which we hereafter refer to as *hmga1a* OE. CMs from this line showed robust nuclear protein localization 14 days post tamoxifen (dpT) (Fig. 5a,b). To investigate transcriptional changes, we sorted CMs from *hmga1a* OE and control *Tg(myl7:CreERT2)* fish at 14 dpT and performed bulk mRNA sequencing (mRNA-seq). Analysis of the mRNA-seq data identified 1,280 upregulated genes ($P < 0.05$, logFC > 1) and 1,203 downregulated genes ($P < 0.05$, logFC < −1) in *hmga1a* OE CMs (Extended Data Fig. 5a and Supplementary Table 9). There was a striking correlation between the upregulated genes and the scRNA-seq modules 5–8, containing BZ genes downstream of Hmga1a, and between the downregulated genes with scRNA-seq modules 1–4, which contain genes upstream of Hmga1a (Extended Data Fig. 5b,c). In addition, a comparison with previously identified BZ genes[5] revealed that 28% of these BZ genes were upregulated in *hmga1a* OE CMs (Extended Data Fig. 5d,e). Together, this suggests that *hmga1a* OE stimulates a more embryonic-like BZ transcriptome.

Next, we quantified the fraction of proliferating cell nuclear antigen (PCNA)$^+$ CMs at 14 dpT of *hmga1a* OE to investigate the consequences of the Hmga1a-induced transcriptional changes on CM proliferation. We observed that Hmga1a OE resulted in a significant induction of PCNA$^+$ CMs, without affecting sarcomere organization or heart morphology (Fig. 5b–d). Long-term Hmga1a OE for 1 year affected cardiac growth, as we observed a significant increase in myocardial surface area (Fig. 5e,f), mainly due to an expansion of the trabecular region at the expense of the cardiac lumen (Fig. 5g,h). This expansion was due to the modest but significant increase in CM proliferation (Fig. 5i), not due to an increase in CM size (Fig. 5j). Notably, although hearts from long-term *hmga1a* OE fish displayed enhanced growth, they did not show any pathological remodeling (Fig. 5k), which is a striking difference when compared to 5 months of Nrg1 OE in *Tg(β-actin2:loxPmTagBFP-STOP-loxP-Nrg1)* zebrafish (Fig. 5l). Together, these results demonstrate that *hmga1a* OE in CMs is sufficient to induce a partial BZ-like gene expression program, including the induction of CM proliferation without any pathological consequences.

Epigenetic remodeling by Hmga1a

Given the role of Hmga1 in chromatin organization[44,55,56], we investigated whether the transcriptional changes observed in *hmga1a* OE are associated with changes in epigenetic modifications in CMs. Ex vivo time-lapse imaging on cardiac slices revealed that the nuclear Hmga1a–eGFP remained bound to chromatin during CM division (Extended Data Fig. 6a), indicating that it is a structural chromatin component. To further explore Hmga1a-induced epigenetic changes, we employed sort-assisted single-cell chromatin immunocleavage (sortChIC), a technique combining cell sorting, which allowed us to sort for CMs, with chromatin immunocleavage[57], to map changes in three histone marks: histone 3 lysine 4 trimethylation (H3K4me3) (marking active promotors), histone 3 lysine 9 trimethylation (H3K9me3) (marking constitutive heterochromatin) and H3K27me3 (marking facultative heterochromatin) (Fig. 6a). As expected, we found that H3K4me3 was enriched at promoter regions, H3K9me3 at distal intergenic regions and H3K27me3 in intergenic regions, gene bodies and promoter regions (Fig. 6b and Extended Data Fig. 7a). Additionally, gene expression levels correlated with H3K4me3 and H3K27me3 marks: highly expressed genes showed high H3K4me3 levels and low H3K27me3 levels (Fig. 6b). In contrast, no such correlation was observed for H3K9me3, likely due to its predominant localization in intergenic regions (Extended Data Fig. 7a,b). Comparing *hmga1a* OE and control CMs, we observed a significant increase in H3K4me3 marks on promoter regions and a significant decrease in H3K27me3 marks on gene bodies in *hmga1a* OE CMs (Fig. 6c). To further assess whether *hmga1a* OE affects H3K27me3 levels, we performed immunohistochemistry on tissue sections of zebrafish hearts. We observed a significant reduction of H3K27me3 levels in zebrafish hearts with *hmga1a* OE compared to controls (Fig. 6d,e), demonstrating that *hmga1a* OE reduces repressive H3K27me3 marks, potentially leading to increased gene expression. Indeed, analysis of H3K27me3 levels on gene bodies in a subset of genes upregulated by *hmga1a* OE showed a strong and significant reduction in H3K27me3, whereas genes downregulated by *hmga1a* OE did not exhibit such a reduction (Fig. 6f).

https://doi.org/10.1038/s44161-024-00588-9

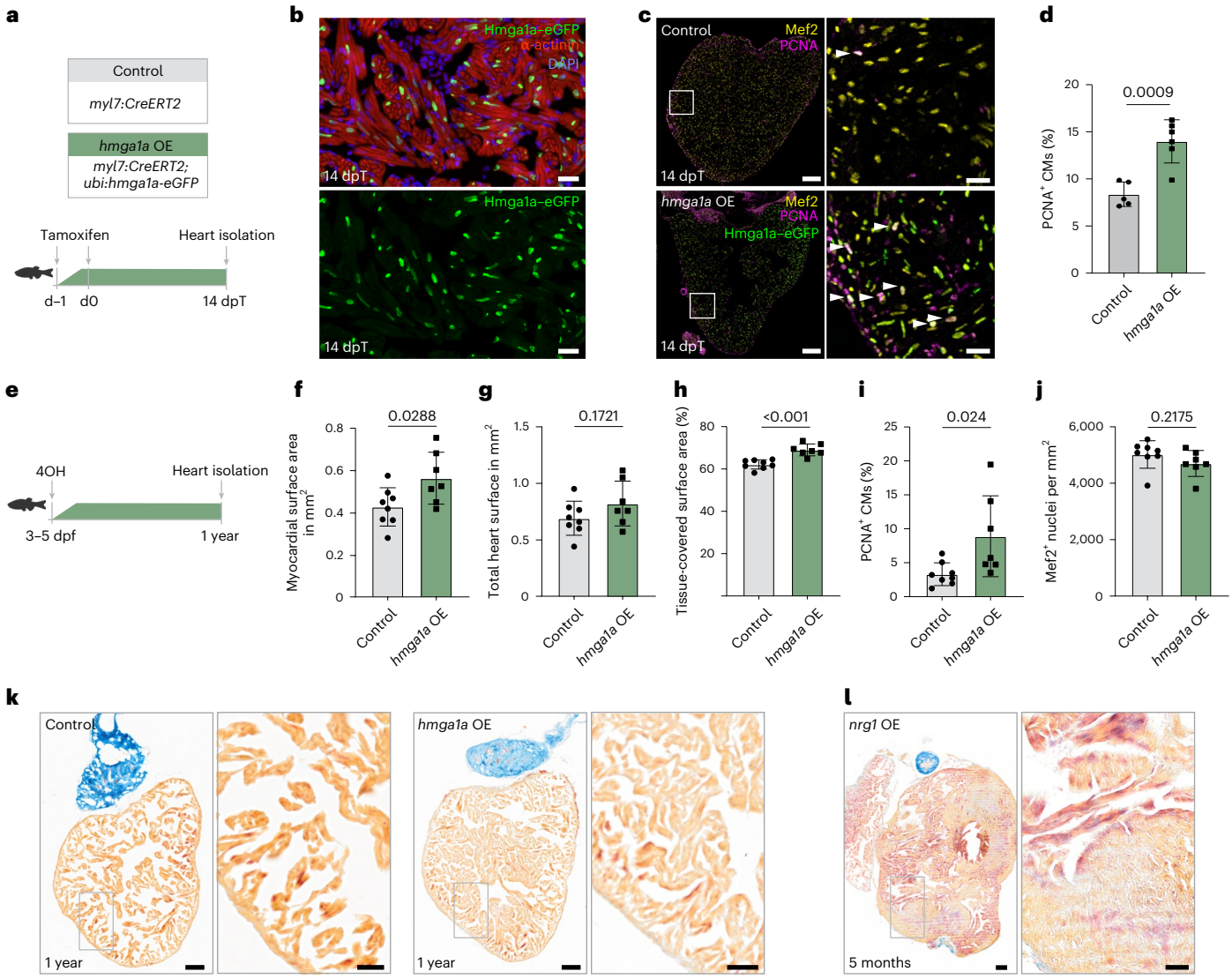

Fig. 5 | *hmga1a* OE stimulates CM proliferation resulting in myocardial expansion without pathological remodeling. a, Workflow of tamoxifen treatment for 14 days of *hmga1a* OE used in **b**–**d**. **b**, Representative images of immunofluorescent staining for GFP, α-actinin and DAPI on a *Tg(ubi:Loxp-stop-Loxp-hmga1a-eGFP, myl7:CreERT2)* heart at 14 dpT. $n = 6$ hearts were analyzed. CM-specific nuclear Hmga1a–eGFP can be observed in most CMs. Scale bars, 20 µm. **c**, Representative images of immunofluorescent staining against Mef2, PCNA and Hmga1a–eGFP on 14-dpT control and *hmga1a* OE hearts. Arrowheads indicate proliferating CMs. Overview scale bars, 100 µm; zoom-in scale bars, 20 µm. **d**, Quantification of proliferating CMs in control ($n = 5$) and *hmga1a* OE ($n = 6$) hearts at 14 dpT. Datapoints represent individual hearts. Error bars indicate mean ± s.d. Statistics were performed by two-tailed unpaired *t*-test and show a significant difference between control and *hmga1a* OE ($P = 0.0009$). **e**, Workflow of tamoxifen treatment for long-term *hmga1a* OE used in **f**–**k**. dpf, days post fertilization; 4OH, 4-hydroxytamoxifen. **f**–**j**, Quantification of differences between control ($n = 8$) and *hmga1a* OE ($n = 9$) hearts, including myocardium-covered surface area ($P = 0.0288$) (**f**), total heart surface (myocardium + lumen) ($P = 0.1721$) (**g**), the percentage of total heart surface covered with myocardium ($P < 0.001$) (**h**), the percentage of proliferating CMs ($P = 0.024$) (**i**) and the density of cardiomyocyte nuclei ($P = 0.2175$) (**j**). Datapoints represent individual hearts. Error bars indicate mean ± s.d. Statistics were performed using two-tailed unpaired *t*-tests. **k**,**l**, Representative images of AFOG staining on a 1-year control and *hmga1a* OE zebrafish heart (**k**) and a 5-month *nrg1* OE *Tg(β-actin2:loxPmTagBFP-STOP-loxP-Nrg1)* heart (**l**) showing muscle in orange, fibrin in red and collagen in blue. $n = 8$ control, $n = 9$ *hmga1a* OE and $n = 1$ *nrg1* OE hearts were analyzed. Scale bars, 100 µm in the overviews and 50 µm in the zoom-ins.

Among the genes both downstream of Hmga1a and upregulated by *hmga1a* OE, as revealed by our RNA-seq analyses, are embryonic cardiac genes (for example, *nppa*), cardiac transcription factors (for example, *nkx2.5* and *tbx20*) and genes with a role in energy metabolism (for example, *aldoab* (aldolase a, fructose-bisphosphate, b) and *mb* (myoglobin)). Genome track of these genes revealed a clear correlation among a reduced H3K27me3 signal over the gene body and promoter region, an increased H3K4me3 signal at the promoter region and increased mRNA reads upon *hmga1a* OE (Fig. 6g). Conversely, genome tracks of genes such as *hox* genes show no reduction in H3K27me3 levels upon *hmga1a* OE (Extended Data Fig. 7c), highlighting the specificity of *hmga1a* OE. Together, these results support a model in which *hmga1a* OE leads to a reduction in H3K27me3 and an increase in H3K4me3 on genes involved in cardiac development and energy metabolism, resulting in upregulation of these genes.

Hmga1 stimulates mammalian heart regeneration

Given the observed effects of *hmga1a* OE in zebrafish, we tested the potential of Hmga1 to stimulate mammalian heart regeneration. Because the neonatal mammalian heart can regenerate, and neonatal CMs are susceptible to proliferative stimuli[8,58,59], we addressed whether ectopic Hmga1 expression in primary isolated neonatal rat ventricular

https://doi.org/10.1038/s44161-024-00588-9

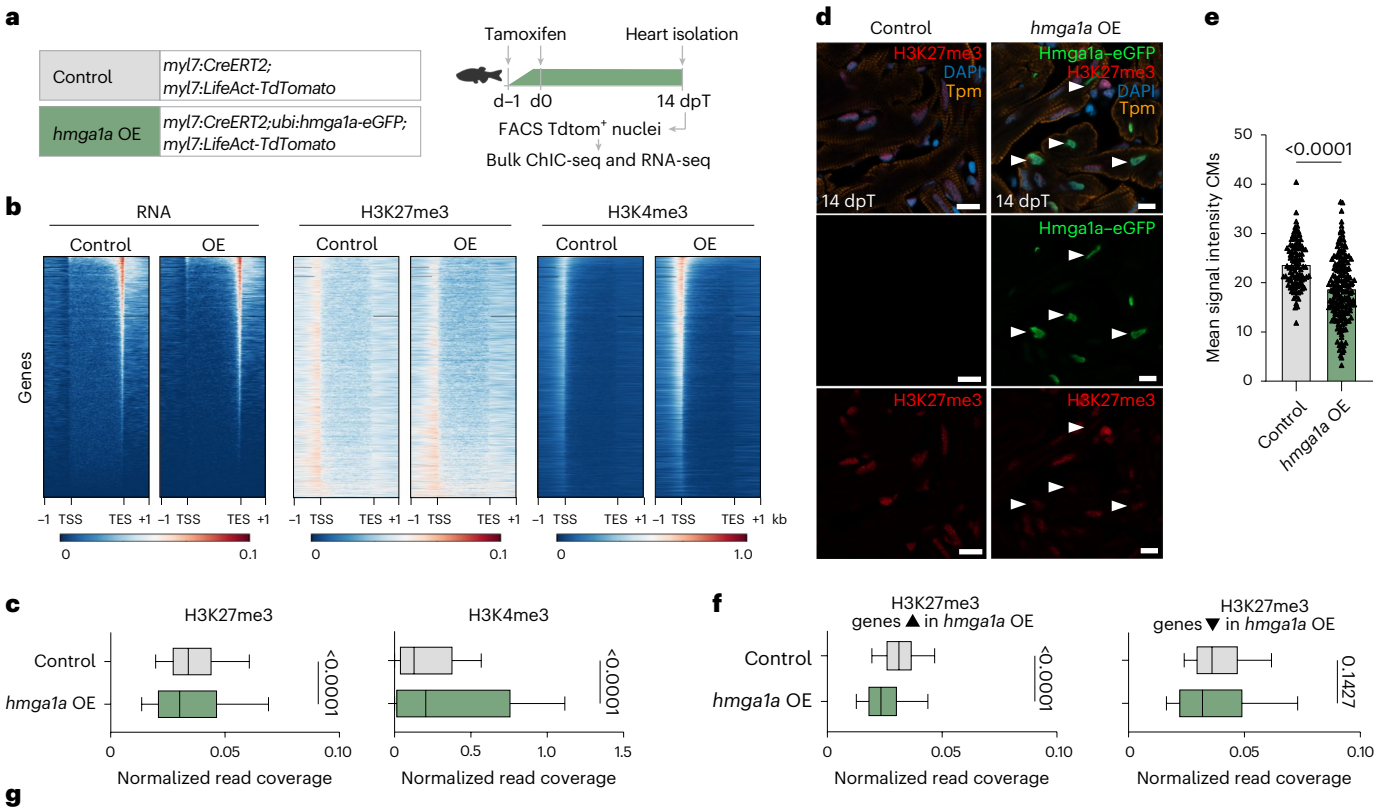

Fig. 6 | Reduction of repressive H3K27me3 marks by *hmga1a* OE in zebrafish CMs. a, Schematic overview for bulk sortChIC (control $n = 10$, *hmga1a* OE $n = 10$) and RNA-seq (control $n = 14$, *hmga1a* OE $n = 14$). **b**, Heatmap showing read distribution of RNA expression and levels of H3K27me3 and H3K4me3 in control and *hmga1a* OE CMs. TSS, transcription start site; TES, transcription end site; −1 and +1 indicate the kilobase distance from TSS or TES. **c**, Quantification of histone mark levels on all genes, comparing normalized read coverage in control versus *hmga1a* OE CMs. H3K27me3 levels (peak data on $n = 21{,}440$ genes) are significantly reduced on gene bodies ($P < 0.001$), and H3K4me3 levels (peak data on $n = 21{,}843$ genes) are significantly increased on promoter regions in *hmga1a* OE CMs ($P < 0.001$). Center line indicates median; whiskers indicate 10th/90th percentiles. Statistics were performed using two-tailed unpaired *t*-tests. **d**, Representative images of immunofluorescent staining for H3K27me3, tropomyosin (Tpm), Hmga1a−eGFP and DAPI on 14-dpT control and *hmga1a* OE hearts. Arrowheads indicate Hmga1a−eGFP$^+$ CMs with low H3K27me3. Scale bars, 5 µm. **e**, Quantification of H3K27me3 signal intensity in single CMs of 14-dpT control ($n = 8$) versus *hmga1a* OE ($n = 8$) hearts. Datapoints represent single CM nuclei measured. Error bars indicate mean ± s.d. Statistics were performed using a one-way ANOVA followed by Tukey's multiple comparisons test and show a significant difference ($P < 0.0001$). **f**, Quantification of H3K27me3 levels on genes upregulated in *hmga1a* OE CMs (peak data on $n = 1{,}141$ genes) and genes downregulated in *hmga1a* OE CMs (peak data on $n = 1{,}001$ genes), comparing normalized read coverage in control versus *hmga1a* OE CMs. H3K27me3 levels were significantly reduced on gene bodies ($P < 0.001$) of genes upregulated in *hmga1a* OE CMs but not significantly different between control and *hmga1a* OE CMs on gene bodies of genes downregulated upon *hmga1a* OE. Center line indicates median; whiskers indicate 10th/90th percentiles. Statistics were performed using two-tailed unpaired *t*-tests. **g**, Genome tracks of example genes that were significantly upregulated in 14-dpT *hmga1a* OE CMs and were found downstream of Hmga1a (modules 5–8 in the scRNA-seq).

cardiomyocytes (NRVMs) stimulates proliferation (Extended Data Fig. 8a). Interestingly, a significant increase in 5-ethynyl-2′-deoxyuridine (EdU) incorporation and Ki67 labeling was observed in the Hmga1–eGFP transduced NRVMs compared to the eGFP-only transduced CMs (Extended Data Fig. 8b,c), indicating that delivery of Hmga1 in neonatal mammalian CMs can increase their proliferative capacity.

https://doi.org/10.1038/s44161-024-00588-9

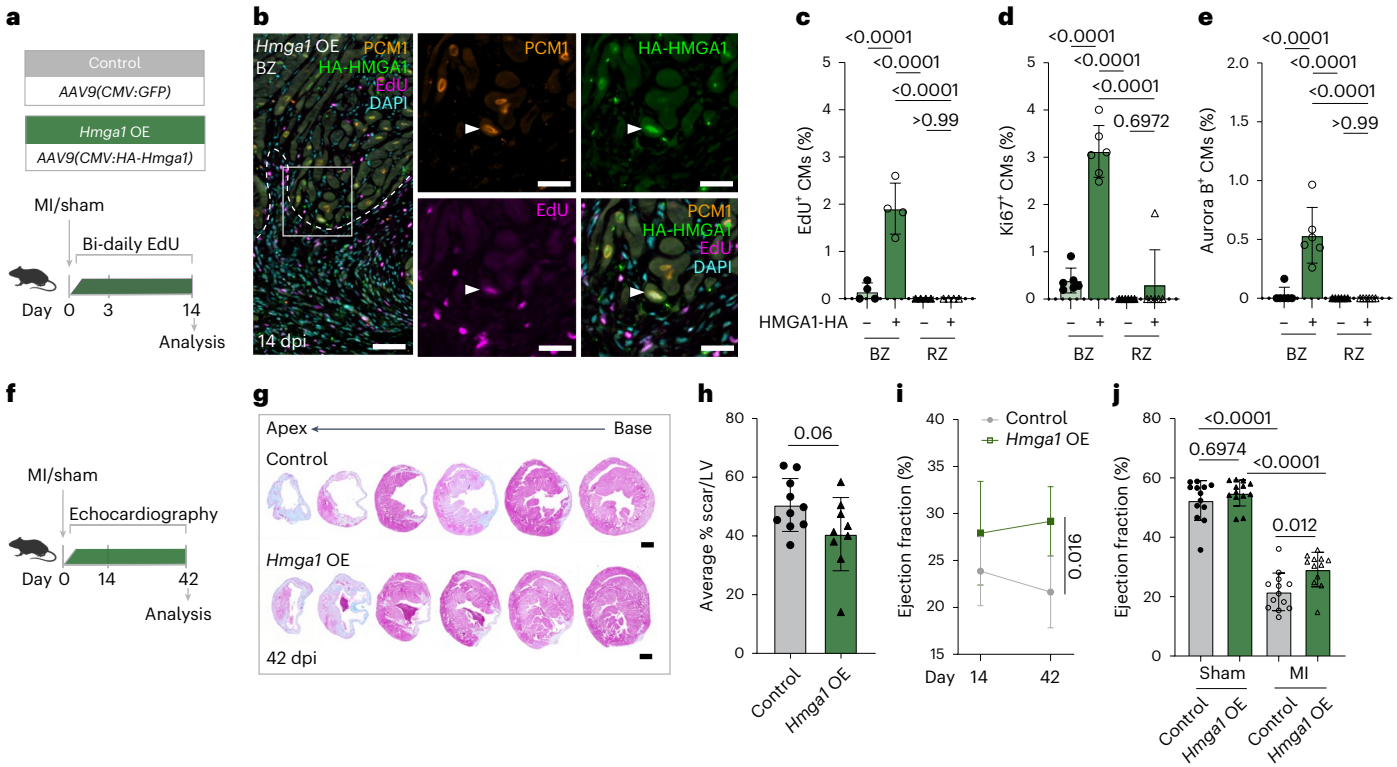

Fig. 7 | HMGA1 promotes CM proliferation and cardiac regeneration in injured adult mice. a, Schematic overview for experiments in **b**–**e**. **b**, Representative image of immunofluorescent staining against PCM-1, HA and EdU. Dashed line indicates the injury border. Arrowheads indicate HMGA1-HA$^+$EdU$^+$ CMs. Scale bars, 100 µm in overview and 20 µm in zoom-in. **c**–**e**, Quantification of EdU$^+$ (**c**), Ki67$^+$ (**d**) and Aurora B$^+$ (**e**) CMs within the BZ and RZ of hearts transduced with HA-HMGA1. $n = 4$ hearts were analyzed for EdU and $n = 6$ for Ki67/Aurora B quantification. Datapoints represent individual hearts. Error bars indicate mean ± s.d. Statistics were performed using a one-way ANOVA followed by Tukey's multiple comparisons test and show significant differences for % EdU$^+$/Ki67$^+$/AuroraB$^+$ CMs in HMGA1-HA$^+$ BZ CMs compared to HA$^-$ BZ CMs and RZ HA$^{+/-}$ CMs ($P < 0.0001$ for all). No significant difference was found between RZ HA$^-$ and HA$^+$ cells for % EdU$^+$ CMs ($P > 0.99$), % Ki67$^+$ CMs ($P = 0.6972$) and % AuroraB$^+$ CMs ($P > 0.99$). **f**, Workflow for mouse experiments in **g**–**j**. **g**, Representative images of control and *Hmga1* OE hearts at 42 dpi stained with Masson's trichrome. Distance between sections is 400 µm. Scale bars, 1 mm. **h**, Quantification of scar size in control ($n = 10$) and *Hmga1* OE ($n = 9$) hearts at 42 dpi showing average % MI length/midline LV length. Error bars indicate mean ± s.d. Statistics were performed by two-tailed unpaired *t*-test and show no significant difference ($P = 0.06$). **i**, Quantification of EF at 14 dpi and 42 dpi of control ($n = 13$) and *Hmga1* OE ($n = 13$) hearts. Error bars indicate mean ± s.d. Statistics were performed using a two-way ANOVA followed by Sidak's multiple comparisons test and show a significant difference ($P = 0.016$). **j**, Quantification of EF at 42 dpi of sham ($n = 13$ control, $n = 13$ *Hmga1* OE) and MI ($n = 13$ control, $n = 12$ *Hmga1* OE) hearts. Datapoints represent individual hearts. Error bars indicate mean ± s.d. Statistics were performed using a one-way ANOVA followed by Tukey's multiple comparisons test and show a significant difference between control sham/MI hearts ($P < 0.0001$), between *Hmga1* OE sham/MI hearts ($P < 0.0001$) and between control and *Hmga1* OE MI hearts ($P = 0.01$) but not between control and *Hmga1* OE sham hearts ($P = 0.6974$).

Although the adult mammalian heart does not regenerate, and BZ CMs display very limited cell cycle activation upon injury, BZ CMs do undergo drastic changes in terms of their morphology[27–29] as well as their transcriptome and chromosomal organization[30], which might potentiate their susceptibility to mitogenic stimuli[10,11,35,60,61]. To address whether introducing Hmga1 expression in injured adult mouse hearts induces CM cell cycle re-entry in vivo, we performed permanent left anterior descending artery (LAD) ligation to induce an MI and injected an adeno-associated virus 9 (AAV9) carrying a control *CMV:GFP* (referred to as *GFP* virus) or a *CMV:HA-Hmga1* cassette (referred to as *Hmga1* virus) in two opposing regions bordering the area at risk of ischemic injury. Co-staining with anti-pericentriolar material 1 (anti-PCM1), which marks the nuclear membrane of CMs, revealed that 95–100% of transduced cells were CMs (Extended Data Fig. 8d), and the intracardiac injection resulted in transduction of 20–30% of all CMs in the BZ (Extended Data Fig. 8e). To assess CM cell cycle activity, mice were injected with EdU bi-daily for 2 weeks after MI (Fig. 7a). At 14 days after MI, EdU incorporation in CMs located at the BZ was increased more than 10-fold in CMs expressing HA-HMGA1 (Fig. 7b,c). In addition, HA-HMGA1 expression in BZ CMs resulted in a more than nine-fold increase Ki67$^+$ CMs and a 10-fold increase in Aurora B$^+$ CMs, further validating that *Hmga1* virus injection induces CM cell cycle re-entry and progression through mitosis and cytokinesis in BZ CMs (Fig. 7d,e and Extended Data Fig. 9a,b). Notably, the percentage of EdU$^+$, Ki67$^+$ or Aurora B$^+$ CMs was not affected in hearts injected with *GFP* virus (Extended Data Fig. 9c–e). Contrary to the observations in the BZ, we did not observe a stimulatory effect of the Hmga1 virus for these cell cycle markers in the CMs located in the RZ (Fig. 7c–e) nor did we observe an induction of CM proliferation in sham-operated hearts (Extended Data Fig. 9f,g), suggesting that, in the mouse heart, the BZ creates a microenvironment that allows HMGA1-induced cell cycle reactivation of CMs. Immune cells, including macrophages, accumulate in the BZ, and their presence is required for CM proliferation during zebrafish and neonatal heart regeneration[33,62]. As *Hmga1* OE can exacerbate inflammation[63], we investigated whether *Hmga1* OE had a similar effect on MI-induced inflammation, but we did not find any evidence for this (Extended Data Fig. 8f–h).

Next, we addressed whether injection of *Hmga1* virus also leads to functional improvement after MI (Fig. 7f). Histological analysis to assess scar size at 42 dpi revealed a modest decrease in scar size in *Hmga1* virus-injected hearts compared to control, albeit not significant (Fig. 7g,h). Sham and MI mice injected with virus were subjected to

https://doi.org/10.1038/s44161-024-00588-9

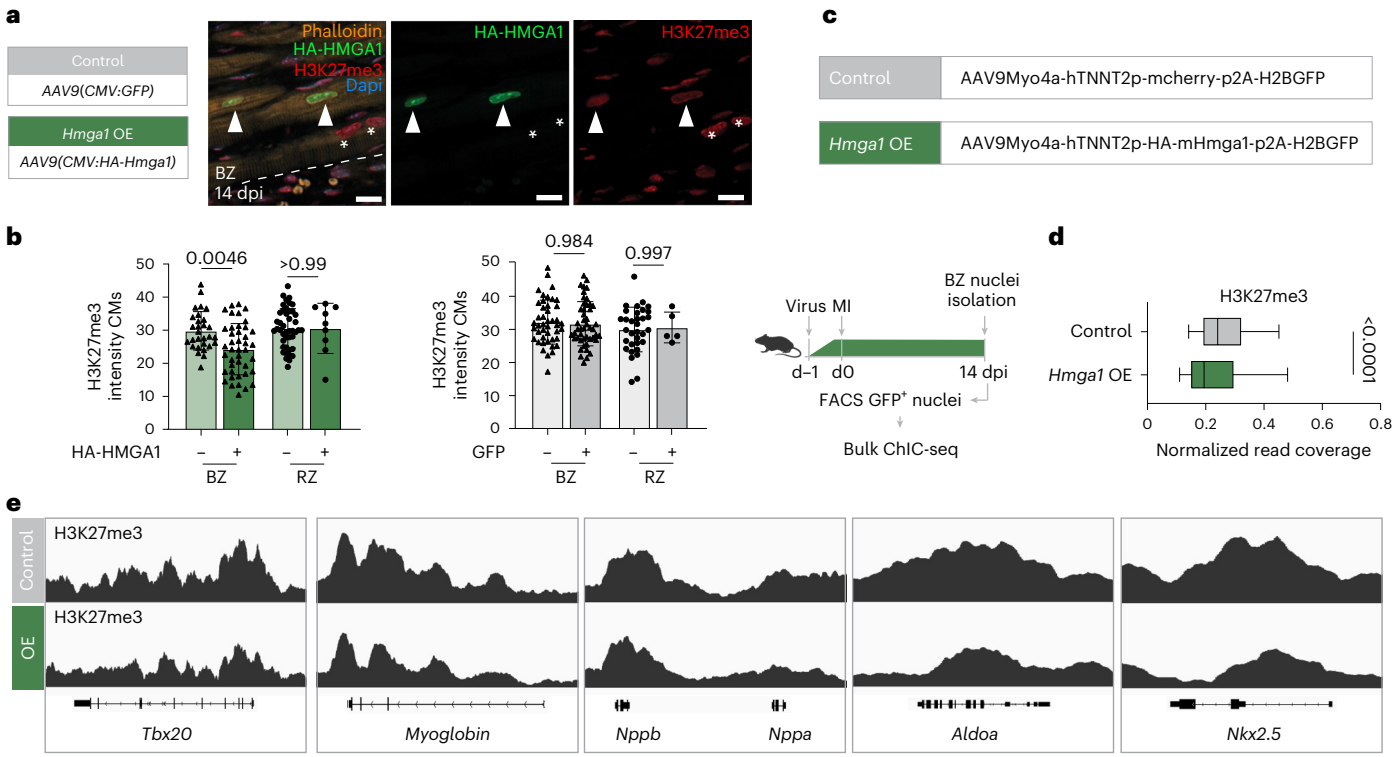

Fig. 8 | Reduction of repressive H3K27me3 marks by HMGA1 in mouse BZ CMs. a, Schematic overview of experiments (**a**,**b**) and representative image of immunofluorescent staining against H3K27me3, HMGA1-HA, phalloidin and DAPI on 14-dpi mouse hearts transduced with *AAV9(CMV:HA-Hmga1)*. Dashed line indicates the injury border. Arrowheads indicate HMGA1-HA transduced CMs; asterisks indicate non-transduced CMs. Scale bar, 5 µm. **b**, Quantification of H3K27me3 signal intensity in single CMs in the BZ and RZ of 14-dpi *Hmga1* ($n = 4$) and *GFP* ($n = 4$) virus transduced hearts. Datapoints represent single CM nuclei measured. Error bars indicate mean ± s.d. Statistics were performed using a one-way ANOVA followed by Tukey's multiple comparisons test and show a significant difference between HA^+ BZ CMs and HA^- BZ CMs ($P = 0.0046$). **c**, Schematic overview for bulk sortChIC on *Hmga1* OE CMs (**c**–**e**). **d**, Quantification of H3K27me3 levels on all genes, comparing normalized read coverage in control versus *Hmga1* OE BZ CMs. H3K27me3 levels (peak data on $n = 21{,}937$ genes) are significantly reduced on gene bodies ($P < 0.0001$) in *Hmga1* OE BZ CMs. Center line indicates median; whiskers indicate 10th/90th percentiles. Statistics were performed using a two-tailed unpaired *t*-test. **e**, Genome tracks of orthologs to example genes in Fig. 6g that are significantly upregulated in 14-dpT *hmga1a* OE CMs and were found downstream of Hmga1a (modules 5–8 in the scRNA-seq). Tracks show reduced H3K27me3 levels on genes in *Hmga1* OE BZ CMs.

echocardiography at baseline, 14 dpi and 42 dpi. At 14 dpi, there was no significant difference in ejection fraction (EF) between *GFP* and *Hmga1* virus-treated animals, but, at 42 dpi, the EF of *Hmga1* virus-treated animals was significantly improved, whereas the EF of *GFP* virus-treated animals continued to decline (Fig. 7i,j). Interestingly, cardiac output and stroke volume improved to sham levels in MI mice injected with *Hmga1* virus (Extended Data Fig. 9h–j). No difference in heart weight or CM size was detected after *Hmga1* OE (Extended Data Fig. 9k–m). Together, these results indicate that a single local injection of *Hmga1* virus in the adult mouse heart after MI promotes mammalian heart regeneration by inducing cell cycle re-entry of BZ CMs and improving cardiac function.

Epigenetic remodeling by Hmga1 in the mouse BZ

Because HMGA1 binds to chromatin in mouse cells[64], a finding that we confirmed (Extended Data Fig. 6b), we investigated whether *Hmga1* OE in mouse hearts leads to similar epigenetic changes as observed in zebrafish hearts with *hmga1a* OE. We first performed immunohistochemistry for H3K27me3 on tissue sections of MI mouse hearts injected with either *GFP* or *Hmga1* virus. Notably, we observed a specific and significant reduction of H3K27me3 levels in BZ CMs of injured mouse hearts expressing HA-HMGA1 (Fig. 8a,b). To further explore whether this reduction in H3K27me3 levels occurs at specific genomic loci, we performed sortChIC on GFP^+ BZ CM nuclei isolated from 14-dpi hearts of mice injected with control (AAV9Myo4a-hTNNT2p-mCherry-p2A-H2BGFP) or *Hmga1* OE (AAV9Myo4a-hTNNT2p-HA-mHmga1-p2A-H2BGFP) virus, which allow sorting on H2B GFP (Fig. 8c). Similar as in zebrafish, we found that H3K27me3 was enriched in intergenic regions, gene bodies and promoter regions (Extended Data Fig. 10a). Comparing H3K27me3 levels between control and *Hmga1* OE BZ CMs, we observed a significant decrease in H3K27me3 marks on gene bodies in *Hmga1* OE CMs (Fig. 8d). Interestingly, analyzing a subset of genes orthologous to genes upregulated or downregulated in zebrafish *hmga1a* OE CMs revealed a significant reduction of H3K27me3 levels upon *Hmga1* OE for genes upregulated but not for those downregulated upon *hmga1a* OE (Extended Data Fig. 10b). Genome tracks for *Tbx20*, *Mb*, *Nppa*, *Aldoa* and *Nkx2.5* showed this reduction in H3K27me3 levels (Fig. 8e). Similar to our observations in the zebrafish, *Hox* genes did not exhibit this reduction in H3K27me3 marks, indicating a level of specificity in the effect of *Hmga1* OE (Extended Data Fig. 10c). These results indicate that *Hmga1* OE reduces repressive H3K27me3 marks from specific genomic loci in mammalian CMs.

Taken together, our data bring forward a model where Hmga1 reduces repressive H3K27me3 marks on developmental genes, thereby allowing for transcription initiation, which ultimately leads to increased CM proliferation and heart regeneration (Extended Data Fig. 10d).

Discussion

CM proliferation has long been a focal point of research owing to its potential in regenerating lost CMs after heart injury[58]. Our study underscores the value of comparing regenerative and non-regenerative species to unveil critical mechanisms and regulators of CM proliferation.

Our findings highlight the pivotal role of Hmga1a in zebrafish as both necessary and sufficient for promoting CM proliferation and regeneration. Furthermore, analysis of epigenetic modifications suggests that Hmga1a acts on the chromatin by effectively removing repressive H3K27me3 marks on genes typically constrained to developmental stages, thereby inducing a pro-regenerative gene expression program. In contrast, *Hmga1* expression in mammals is restricted to neonatal hearts during the regenerative window, with its absence in the adult injured heart. Our research reveals that introducing *Hmga1* expression in the injured adult mouse heart activates a regenerative response, leading to CM proliferation specifically within the BZ. Moreover, a reduction in repressive H3K27me3 marks could be observed in BZ CMs upon *Hmga1* OE, reminiscent of that found in zebrafish.

Diverse roles for Hmga1-driven chromatin organization and gene regulation have been postulated, showing both activating and repressive effects in different contexts[43–46,65–68]. One proposed mechanism by which Hmga1 may influence chromatin state and gene expression is by displacing the linker histone H1 from chromatin[44,55,56]. Histone H1 promotes PRC2-mediated H3K27me3 enrichment and chromatin condensation[69,70]. The displacement of histone H1 results in chromatin opening and a reduction in repressive H3K27me3 marks[47]. Furthermore, after embryonic development, overall H3K27me3 levels rise, which is linked to silencing of developmental genes and enabling cell differentiation[71]. In addition, PRC1/2-mediated repression is known to target transcription factors with crucial roles in development, such as those from *Gata* and *Tbx* transcription factor families[72]. Together, this aligns with our in vivo observation where Hmga1 reduces H3K27me3 marks from chromatin in both zebrafish and mouse CMs, leading to the re-expression of embryonic genes, the reactivation of the cell cycle and ultimately heart regeneration. Indeed, the injection of a virus expressing EZH1, a catalytic subunit of the PRC2 complex, in mouse hearts after an MI results in a genome-wide reduction of H3K27me3 and an increase in H3K27me1 chromatin marks in CMs, promoting heart regeneration[73]. However, expression of a mutant histone $H3.3^{k27m}$ in adult zebrafish heart impairs heart regeneration independently from CM cell cycle re-entry[74], likely due to a reduction in both H3K27me1 and H3K27me3. It is worth noting that prolonged depletion of H3K27me3 from developmentally regulated genes may affect not only proliferation but also CM redifferentiation and maturation, crucial for successful regeneration[16,26]. The precise mechanisms conferring the specificity of Hmga1 in gene regulation remain to be fully elucidated, but they may involve specific post-translational modifications, such as phosphorylation and acetylation[42,67,73,74], and interactions with chromatin transcriptional regulators, such as chromatin remodeling complexes and transcription factors[42,67,75].

The introduction of Hmga1 in mouse hearts via intramyocardial AAV9-mediated delivery resulted in CM cell cycle re-entry in the BZ but not in transduced CMs in the RZ or uninjured hearts. In contrast, Hippo inactivation[9] or ErbB2 activation[11] induces CM cell cycle re-entry also in remote myocardium and even in uninjured mouse hearts. The BZ-specific effect of Hmga1-induced CM proliferation might be aided by the general susceptibility of mouse BZ CMs to mitogenic stimuli[10,35,60,61]. In addition, due to the use of the CMV promoter Hmga1, transduction of non-CMs and subsequent cell–cell signaling might contribute to the induced CM proliferation, although low non-CM transduction rate makes this unlikely. Furthermore, differences in immune response and fibroblast activation in the BZ versus the remote myocardium might provide a permissive microenvironment for the pro-proliferative effect of Hmga1 (refs. 76,77). This distinction holds promise in clinical applications, as Hmga1-induced proliferation would naturally cease once the permissive BZ microenvironment has resolved[30], preventing uncontrolled CM proliferation, cardiomegaly and adverse remodeling, issues that have plagued previous strategies[11,13–15,18]. Remarkably, *Hmga1* OE is sufficient to improve cardiac function of the left ventricle (LV), underscoring its pro-regenerative effect in the mammalian heart.

Finally, we acknowledge several limitations of our study. Although sortChIC provided valuable insight into epigenetic marks in the context of ectopic *hmga1a/Hmga1* expression in zebrafish as well as mouse, it did not allow us to directly compare histone marks on BZ CMs in zebrafish and mouse due to technical constraints. Additionally, to fully elucidate the role of Hmga1 in epigenetic regulation, we need to optimize techniques to map Hmga1 binding sites in zebrafish as well as mouse CMs, which is a priority for future experiments. Finally, although we demonstrated that *Hmga1* OE stimulates CM proliferation only in the context of an injury, this suggests that an injury-induced signal cooperates with Hmga1 to reduce H3K27me3 marks and induce CM proliferation. Identifying the nature of this injury-induced signal will be key to understanding the full mechanism by which Hmga1 drives cardiac regeneration.

In conclusion, this study underscores the pivotal role of Hmga1 in driving CM proliferation and regeneration in both zebrafish and mice, offering promising prospects for regenerative therapies.

Methods

Animal experiments

All procedures involving animals were approved by the Animal Welfare Body of the Royal Dutch Academy of Sciences and Arts and were performed in compliance with animal welfare laws, guidelines and policies, according to national and European law.

Zebrafish and mouse lines

The following zebrafish lines were used: TL, TgBAC(nppa:mCitrine)[5], $Tg(myl7:CreER)^{pd10}$ (ref. 23), Tg(myl7:DsRed2-NLS)[79], Tg(myl7:LATdTomato) and Tg(β-actin2:loxPmTagBFP-STOP-loxP-Nrg1)[52]. Both males and females were used for zebrafish experiments. The $khdrbs1a^{-/-}$ and $znfx1^{-/-}$ were produced using CRISPR–Cas9-based strategies to introduce, respectively, a 14-base pair (bp) deletion in exon 3 of khdrbs1a and, for znfx1, a 4-bp deletion in exon 1, causing a frameshift and pre-mature stop codon. The $hmga1a^{-/-}$ was produced using a TALEN-based strategy, targeting the region adjacent to the transcription start site. The resulting 8-bp deletion directly after the start codon caused a frameshift and introduction of a pre-mature stop codon, resulting in a truncated Hmga1a protein (7 amino acids (aa) instead of 101 aa) (Extended Data Fig. 2e). The Tg(ubi:Loxp-stop-Loxp-hmga1a-eGFP) was produced using gBlocks and Gibson Assembly, using the pDESTp3A destination vector[80] and the p5E ubi promotor[81].

The following mouse lines were used: C57BL/6J males (Charles River Laboratories) for all experiments with AAV9-mediated delivery of GFP or Hmga1-HA, *Tg(Nppb:katushka)*[37] for TOMO-seq experiments and C57BL/6N males for experiments with AAV9 Myo4a delivery.

Cryoinjuries in zebrafish

To induce cardiac injury in zebrafish, cryoinjuries were performed on fish of approximately 4–18 months of age. The cryoinjuries were performed as described in ref. 82, with the exception of the use of a copper filament (0.3 mm) cooled in liquid nitrogen instead of dry ice. Animals were excluded from the study in case of signs of aberrant behavior/sickness/infection, according to humane endpoints in animal guidelines.

MI in mice

Experiments with intracardiac injections of AAV9:

Cardiac ischemic injuries were accomplished by permanent occlusion of the LAD, previously described in ref. 37, using adult male mice between 7 weeks and 12 weeks of age. After the mice were anesthetized with a mix of fentanyl (0.05 mg kg^{-1}), midazolam (5 mg kg^{-1}) and dexmedetomidine (0.125 mg kg^{-1}) via intraperitoneal injections, a tracheal tube was placed, and the mouse was connected to a ventilator (Uno Microventilator, UMV-03). Hair was removed from the thorax and neck with VEET ('silk and fresh gevoelige huid') hair removal. The surgical site

was cleaned with iodine and 70% ethanol. Using aseptic techniques with sterile instruments, the skin was incised left of midline to allow access to the third intercostal space (Tough Cut Scissors and Delicate Moria (MC31) forceps). Pectoral muscles were retracted, and the intercostals muscles were cut caudal to the third rib (2× SuperGrip Forceps, Angled). Wound hooks were placed to allow access to the heart. The pericardium was incised longitudinally, and the LAD was identified. A 7–0 silk suture was placed beneath the LAD for MI, followed by intracardiac injection of 2 × 15 µl AAV9. Sham animals only received the intracardiac AAV9 injections. The rib cage was closed with a 5–0 silk suture, and the skin was closed with a wound clip. The animal was disconnected from the ventilator; the tracheal tube was removed; and the animal was placed unrestrained on a nose cone with 100% oxygen in a warm recovery cage until fully ambulatory, at which point the oxygen was turned off. During the whole surgery and recovery, mice were placed on a heating pad of 38–39 °C. To alleviate pain or discomfort, mice were injected subcutaneously with 0.05–0.1 mg kg^{-1} buprenorphine 30 min before surgery as well as 8–12 h after the surgery and 24 h after the surgery.

Experiments with intravenous injections of AAV9Myo4a:

Seven- to nine-week-old male C57BL/6N mice were used for experiments. Mice were injected subcutaneously with buprenorphine (0.075 mg kg^{-1}) and carprofen (0.05 mg kg^{-1}; Rimadyl Cattle) for analgesia at least 30 min before surgery. Anaesthesia was induced with 4% isoflurane in 1 l min^{-1} O_2. Mice were shaved, intubated and placed on a heating pad to maintain body temperature. Intubation was connected to a ventilator (Harvard Apparatus, MiniVent Model 845), and hair removal cream was applied on the surgery area. Subsequently, ropivacaine (3 mg kg^{-1}) was applied subcutaneously at the site of the incision as analgetic. Anaesthesia was maintained using ventilation with 2% isoflurane in 1 l min^{-1} O_2. Left thoracotomy was performed to expose the heart at the third intercostal space. The LAD was identified, and a 8–0 polyamide 6 suture was used to make a permanent ligation for MI. The thoracotomy and skin were closed with a 6–0 reverse cutting needle with a polyamide 6 wire (Ethilon). Post-surgery analgesia consisted of 4 days of ad libitum carprofen (0.06 mg ml^{-1}) in drinking water and high caloric wet food.

Transthoracic echocardiography

Two-dimensional transthoracic echocardiography was performed on sedated (1–2% isoflurane) mice to address heart function, using a VisualSonics ultrasound system with a 30-MHz transducer (VisualSonics). The heart was imaged in a parasternal long-axis as well as short-axis view at the level of the papillary muscles, to record B-mode as well as M-mode measurements and to determine heart rate, wall thickness and end-diastolic and end-systolic dimensions. Fractional shortening (defined as the end-diastolic dimension minus the end-systolic dimension normalized for the end-diastolic dimension) as well as EF (defined as the stroke volume normalized for the end-diastolic volume), cardiac output (defined as amount of blood pumped per minute) and stroke volume (defined as end-diastolic volume minus end systolic volume) were used as an index of cardiac contractile function.

Virus in neonatal rat CMs

Ventricular myocytes of 1-day-old neonatal rat hearts were isolated by enzymatic dissociation with trypsin (Thermo Fisher Scientific, 15400054) and cultured as described in ref. 83. After 2 days of culturing, OE of *GFP/Hmga1* was accomplished through lentivirus-mediated delivery of, respectively, *pHAGE2-EF1a:GFP*/*pHAGE2-EF1a:Hmga1-T2A-GFP* constructs. Cells were fixed and analyzed after two more days.

AAV9 production and injections in mice

Recombinant AAV9 vectors used in this study, carrying a *CMV:GFP* or a *CMV:HA-Hmga1* cassette, prepared by the AAV Vector Unit at the International Centre for Genetic Engineering and Biotechnology Trieste (http://www.icgeb.org/avu-core-facility.html), as described previously[84] with a few modifications. In brief, infectious AAV vector particles were generated in HEK293T cells (American Type Culture Collection) cultured in roller bottles by a three-plasmid transfection cross-packaging approach, whereby the vector genome was packaged into AAV capsid serotype-9 (ref. 85). Purification of viral particles was obtained by PEG precipitation and two subsequent $CsCl_2$ gradient centrifugations[86]. The physical titer of recombinant AAVs was determined by quantifying vector genomes (vg) packaged into viral particles, by real-time PCR against a standard curve of a plasmid containing the vector genome[87]; values obtained were in the range of 1×10^{13} to 1×10^{14} vg per milliliter. Directly after LAD ligation during MI surgery, hearts were injected twice with 15 µl of AAV9(*CMV:GFP)* or AAV9(*CMV:HA-Hmga1)* (1×10^{12} virus particles per mouse) in opposing regions bordering the area at risk of ischemic injury.

For the ChIC experiment using AAV9 Myo4a, AAV9Myo4a-hTNNT2p-mCherry-p2A-H2BGFP and AAV9Myo4a-hTNNT2p-HA-mHmga1-p2A-H2BGFP were produced in the Academic Medical Center Amsterdam. One day before LAD, mice were injected into the retro-orbital sinus with 1×10^{11} vg of AAV9Myo4a per animal. For this, animals were anesthetized in an induction chamber with of 4% isoflurane in 1 l min^{-1} O_2. After being fully sedated, the animal was taken out of the chamber, and the thumb and index finger were used to pull back the skin around the eye socket until the eye slightly protruded. A 0.3-ml (30-gauge) × 8-mm U-100 insulin needle (BD Micro-Fine) was inserted at an angle of 45° starting around the medial canthus toward the retro-orbital sinus. The construct was slowly injected in one smooth motion in a maximum volume of 100 µl, after which the animal was placed on a heating pad until it fully regained consciousness.

EdU injections in mice

To assess cell cycle re-entry at 14 days after MI, adult mice received bi-daily intraperitoneal injections of EdU in PBS starting at day 2 (resulting in six EdU injections in total, per mouse). EdU concentrations were determined based on the individual weight of each mouse (50 µg g^{-1}).

Tamoxifen-induced hmga1a OE in zebrafish

To induce OE of Hmga1a in CMs specifically, the *Tg(ubi:Loxp-BFP-stop-Loxp-hmga1a-eGFP)* line was crossed to the *Tg(myl7:CreER)*^{pd10} line. Adult zebrafish (4–12 months) received two overnight pulses of tamoxifen by swimming them in a 4 µM tamoxifen solution in E3 medium.

NRG1 injections in zebrafish

Intraperitoneal injections of human recombinant NRG1 (PeptroTech: recombinant human heregulin-b1, catalog number 100-03) were performed as described in ref. 88. Fish were sedated using tricaine (0.0168%, w/v). Injections were performed using a Hamilton syringe (30-gauge), cleaned before use by washing in 70% ethanol, followed by two washes in PBS. Injection volumes were adjusted on the weight of the fish (30µl g^{-1}), and a single injection contained 60 µg kg^{-1} of human recombinant NRG1 (diluted in PBS/BSA 0.1%).

Live imaging cardiac slices

Live imaging was performed as described previously[89]. Hmga1a OE hearts were extracted 14 dpT, and imaging was performed using a Leica SP8 confocal microscope in a temperature-controlled chamber at 28 °C. z-stacks with a z-step size of 1 µm were acquired every 10 min.

Heart collection for histological analysis

In mice, mouse hearts were isolated and washed in PBS, after which they were fixed in 4% paraformaldehyde (PFA) (room temperature, overnight, on shaker), dehydrated through an ethanol series, embedded in paraffin and sectioned at 6 µm to use for histology.

In zebrafish, adult zebrafish ventricles were isolated and fixed in 4% PFA (4 °C, overnight, on shaker). The next day, the hearts were washed 3 × 10 min in 4% sucrose phosphate buffer, 5 h in 30% sucrose at room temperature and then embedded in cryo-medium (OCT).

Cryo-sectioning of the hearts was performed at 10-µm thickness. For zebrafish paraffin sections, hearts were fixed in 4% PFA (4 °C, overnight, on shaker), followed by dehydration in ethanol series and subsequent paraffin embedding and sectioning at 10-µm thickness.

Human. Paraffin-embedded infarcted human heart tissue from three individuals who had died of MI were retrieved from the pathology archive of the University Medical Center Utrecht. Material was handled in a coded manner that met the criteria of the Code of Conduct used in The Netherlands for the responsible use of human tissue in medical research. Collection of the archive material was approved by the local biobank review committee (protocol 15–252).

ISH

In zebrafish paraffin sections, ISH was performed on paraffin sections as previously described[90] except that the hybridization buffer used did not contain heparin and yeast total RNA. Zebrafish cryosections: ISH was performed as for paraffin; however, sections were pre-fixed for 10 min in 4% PFA + 0.25% glutaraldehyde (Sigma-Aldrich) before Proteinase K treatment. Moreover, slides were fixed for 1 h in 4% PFA directly after staining. Slides were mounted in Entellan (Merck) mounting medium and imaged on either a DM4000 (Leica) or a VS200 Slide Scanner (Olympus). Zebrafish Dig probes were made via PCR for: *hmga1a* using 5′-TACTGTGTCTCGGGGCAAAA-3′ and 5′-GAGtaatacgactcactatagggACCCTTTGAGTGCGAGACAT-3′, *hmga1b* using 5′-CCCATCCAAGAGAAAATCATCGA-3′ and 5′-GAGtaatacgactcactatagggAAGCACCTCAGTCCAATTTAGA-3′, *hk1* using 5′- TGGGTGGCTCTAATTTCCGT-3′ and 5′- GAGattaaccctcactaaagggaAGAGGCATACACTTTGGGCT-3, *znfx1* using 5′-AAATGCTGTCCACCGTCCTA-3′ and 5′-GAGattaaccctcactaaagggaCATGGAGACGGAATGCACAG-3′, *khdrbs1a* using 5′-ATTTCCACCATCGCTCTCCA-3′ and 5′-GAGtaatacgactcactatagggACAGTCAGGAATGGGAGCAA-3′ and *tbx20* using linearized plasmid. Mouse Dig probes were made via PCR for: *Hmga1* using 5′-GGGAAGCAAGAATAAGGGCG-3′ and 5′-GAGtaatacgactcactatagggAAAACAAAGCGCCCAGAGAG-3′, *Rhoc* using 5′-CCGAAAGAAGCTGGTGATCG-3′ and 5′-GAGtaatacgactcactatagggGTGGCCATCTCAAACACCTC-3′, *Fstl1* using 5′-GCCGAGGAAGAGCTAAGGAG-3′ and 5′-GAGtaatacgactcactatagggGAGCTCATCACGGTTGGACT-3′, *Tmsb4x* using 5′-CCGCCAATATGCACTGTACA-3′ and 5′-GAGtaatacgactcactatagggTGGCACTCTGATTAAACTGCA-3′, *Nppa* using 5′-GCATTCCAGCTCCTAGGTCA-3′ and 5′-GAGtaatacgactcactatagggTCAGTACCGGAAGCTGTTACA-3′, *Des* using 5′-GAGCTGCTGGACTTCTCACT-3′ and 5′-GAGtaatacgactcactatagggTCATACTGAGCCCGGATGTC-3′, *Ankrd1* using 5′-GGGGAGCAACAGTGGAAAAG-3′ and 5′-GAGtaatacgactcactatagggTCCTTCTCTGTCTTTGGCGT-3′, *Tnnt2* using 5′-TGTTGAAGAGCAGGAGGAGG-3′ and 5′-GAGtaatacgactcactatagggCTCCTTCTCCCGCTCATTCC-3′ and *Ech1* using 5′-GGGATAGTGGCTTCTCGCAG-3′ and 5′-GAGattaaccctcactaagggaGATAGCCGCAGACTCACCTC-3′.

qPCR

Total RNA was isolated from heart ventricles using TRIzol reagent (Life Technologies) according to the manufacturer's instructions. Total RNA (1 µg) was reverse transcribed using an iScript cDNA Synthesis Kit (Bio-Rad). Real-time PCR was performed using an iQ SYBR Green kit and a CFX96 real-time PCR detection system (Bio-Rad). Data were normalized using reference genes Gapdh (Fig. 3c) or Hprt and Eefe1e (Extended Data Fig. 2c).

Western blot

Protein samples (20 µg per sample) were separated on a 15% SDS-PAGE gel (separation gel: 40% acrylamide, 2% Bis solution, 3 M Tris pH 8.8, MQ, 10% SDS, 10% APS, 1% TEMED; stacking gel: 40% acrylamide, 2% Bis solution, 3 M Tris pH 6.8, MQ, 10% SDS, 10% APS, 1% TEMED). Protein was transferred to methanol-activated PVDF membrane using semi-dry electroblotting with an Amersham Imager 600 (65 mA, 1.5 h). PVDF membrane was incubated in blocking solution (5% BSA in 0.1% TBS-T) for 30 min, after which the membrane was incubated in blocking solution with primary antibody (Abcam Rb mAb HMGA1, AB129153, 1:1,000, and Calbiochem anti-α-tubulin mouse mAb, CP06-100UG, 1:1,000) at 4 °C overnight. PVDF membrane was incubated with secondary antibody (BD Pharmingen HRP goat anti-rabbit, 554021, 1:10,000, and BD Pharmingen HRP goat anti-mouse, 554002, 1:10,000) for 1 h at room temperature. PVDF membrane was imaged using SuperSignal West Pico Chemiluminescence Signal (Thermo Fisher Scientific) on an Amersham ImageQuant 800 western blot imaging system.

Immunohistochemistry

On zebrafish cryosections, antigen retrieval was performed by heating slides containing heart sections at 85 °C in 10 mM sodium citrate buffer (pH 6) for 15 min. Primary antibodies used included anti-PCNA (Dako, M0879, 1:800), anti-GFP (Aves Labs, GFP-1010, 1:1,000), anti-Mef2c (Santa Cruz Biotechnology, sc313, and Biorbyt, orb256682, both 1:1000), anti-phosphor-S6 ribosomal protein (ser235/236) (Cell Signaling Technology, 4858, 1:500), anti-tri-methyl-histone H3 (Lys27) (C36B11) (Cell Signaling Technology, 9733T, 1:300), anti-α-actinin (Sigma-Aldrich, A7811, 1:500) and anti-tropomyosin (Sigma-Aldrich, T9283, 1:500). On mouse paraffin sections, antigen retrieval was performed by heating slides containing heart sections under pressure at 120 °C in 10 mM sodium citrate buffer (pH 6) for 1 h. Primary antibodies used included anti-HA (Abcam, ab9111, or BioLegend, 901501, both 1:200), anti-PCM (Atlas Antibodies, HPA023370, 1:400), anti-tri-methyl-histone H3 (Lys27) (C36B11) (Cell Signaling Technology, 9733T, 1:300), anti-Ki-67 (SolA15) (eBioscience Invitrogen, 15227437, 1:1,000), anti-Aurora B (AIM1) (BD Biosciences, 611082, 1:300), anti-mouse CD45 (BD Biosciences, 53076, 1:200) and anti-rabbit CD68 (Abcam, ab125212, 1:200). EdU was visualized with a Click-iT EdU Cell Proliferation Imaging Kit, Alexa Fluor 647 (Thermo Fisher Scientific, C10340), according to the instructions. For both mouse and zebrafish tissue, secondary antibodies included anti-chicken Alexa Fluor 488 (Thermo Fisher Scientific, A11039, 1:500), anti-mouse Alexa Fluor 488 (Thermo Fisher Scientific, A21133, 1:500), anti-rabbit Alexa Fluor 555 (Thermo Fisher Scientific, A21428, 1:500), anti-mouse Alexa Fluor 555 (Thermo Fisher Scientific, A21127, 1:500), anti-mouse Alexa Fluor 633 (Thermo Fisher Scientific, A21050, 1:500) and anti-mouse Cy5 (Jackson ImmunoResearch, 118090, 1:500). Phalloidin (Merck, P1951, 1:200) was used as an actin marker. Wheat gluten albumin (WGA) was used as a membrane marker (Merck, 100 µg ml^{-1}, 30 min). Nuclei were shown by DAPI (Invitrogen, D1306, 1:1,000). Images of immunofluorescence staining are single optical planes acquired with a VS200 Slide Scanner (Olympus), an Sp8 microscope (Leica) or an LSM900 AiryScan (Zeiss).

Acid fuchsin orange G staining

Zebrafish paraffin sections were rehydrated in dH_2O and post-fixed with Bouin's solution (Sigma-Aldrich) at 60 °C for 2 h. Slides were cooled and rinsed under running water, followed by incubation with 1% phosphomolybdic acid for 2 min, washed in dH_2O and stained in acid fuchsin orange G (AFOG) solution (1:1:1 ratio of analine blue, orange G and acid fuchsin, pH 1.09) for 2 min, rinsed in dH_2O, dehydrated in an ethanol series and mounted in Pertex (Sigma-Aldrich). Slides were imaged on the VS200 Slide Scanner (Olympus).

TOMO-seq

Under a fluorescence stereoscope, injured mouse hearts were isolated, and tissue was selected based on the Katushka signal. Tissue was isolated from the injured hearts ($n = 3$) containing part of the injury, Katushka signal and part of the remote myocardium, respectively. TOMO-seq was conducted as previously described[36]. Mapping was performed against the zebrafish reference assembly version 9 (Zv9) and the mouse reference assembly version 9 (mm9). Analysis was done

based on the $\log_2$-transformed fold change (zlfc) of the *z*-score (number of standard deviations above the mean) of all genes. Bioinformatic analyses were largely performed with R software using custom-written code. Hierarchical cluster analysis on the entire dataset (after *z*-score transformation) was performed on all genes with a peak in more than four consecutive sections (*z*-score > 1). Based on hierarchical clustering analysis, together with maker gene expression (BZ markers *Nppa*, *Nppb* and *Des*), we defined the locations of the IA, the BZ and the RZ within our datasets. Injured zebrafish hearts were isolated and processed as described in ref. 24 to obtain IA, BZ and RZ. To transcriptionally compare the zebrafish and mouse BZ, we first pooled all IA, BZ and RZ regions from the different timepoints into one species-specific dataset per species, resulting in 14 (IA), 43 (BZ) and 43 (RZ) sections in the zebrafish dataset and 14 (IA), 65 (BZ) and 54 (RZ) sections in the mouse dataset. GO analysis was performed on these combined lists using the R package edgeR, which uses generalized linear models (GLMs) and empirical Bayes methods to identify differentially expressed genes[91]. These gene lists were subjected to GO analysis using the online tool DAVID[78]. The transcriptional comparison between the zebrafish and the mouse BZ was performed by plotting the logFC (BZ versus the rest of the tissue) of annotated homologs (11,779 gene pairs) annotated in Ensembl (version 89) in a scatterplot (Fig. 1a,b). Genes with no annotated homolog were excluded from analysis. Genes with multiple annotated homologs were plotted as separate gene pairs. Next, gene pairs were selected using the following thresholds. Upregulated in both the mouse and zebrafish BZ (331 gene pairs): zebrafish logFC > 0.5, $P < 0.05$; mouse: logFC > 0.5, $P < 0.05$. Downregulated in both the mouse and zebrafish BZ (326 gene pairs): zebrafish: logFC < −0.5, $P < 0.05$; mouse: logFC < −0.5, $P < 0.05$. Upregulated in the zebrafish BZ but not the mouse BZ (371 gene pairs): zebrafish: logFC > 0.5, $P < 0.05$; mouse: logFC < 0. Upregulated in the mouse BZ but not the zebrafish BZ (366 gene pairs): zebrafish: logFC < 0; mouse: logFC > 0.5, $P < 0.05$. After determining zebrafish-specific and mouse-specific gene pairs, gene pairs were removed, of which at least one paralogous gene showed expression outside of the selection thresholds, accounting for redundant functions between paralogous genes. These gene pairs were subjected to GO analysis using their mouse name in DAVID. All datasets can be accessed via the TOMO-seq website (http://mouse.genomes.nl/tomoseq/2018).

scRNA-seq

TgBAC(nppa:mCitrine)^{hu8889Tg}-positive cells showing high mCitrine expression were isolated from cryo-injured zebrafish hearts (7 days after injury). From 12 *hmga1a*$^{-/-}$ hearts, 768 cells were isolated. From 12 hmga1a$^{+/+}$ wild-type hearts, 768 cells were isolated. Single-cell sequencing libraries were prepared by Single Cell Discoveries using the SORT-seq protocol[92]. The CEL-Seq2 protocol was used for library preparation[93]. Illumina sequencing libraries were prepared with TruSeq small RNA primers (Illumina) and paired-end sequenced at 75-bp read length on an Illumina NextSeq platform. In total, seven 384-well plates were sequenced containing one cell per well, of which three were obtained from wild-type cells and four from *hmga1a*$^{-/-}$ cells. Mapping was performed against the zebrafish reference genome assembly version 9 (Zv9). Based on the distribution of the $\log_{10}$ total reads plotted against the frequency, we introduced a cutoff at minimally 600 reads per cell to be included for further analysis, which left us with a total of 1,310 cells (653 wild-type and 657 *hmga1a*$^{-/-}$ cells). Next, single-cell data were analyzed using Seurat[94]. The following parameters were used: variable features = all genes, dimensions = 8 and resolution = 0.7. This resulted in the identification of six clusters that were plotted in a two-dimensional UMAP. The Seurat object was subsequently subjected to RNA velocity[49]. For this, reads were re-mapped using STAR mapping[95] to generate a dataset where intronic and exonic reads were separated. RNA velocity subsequently used the ratio of these reads to generate a vector that predicts the future state of a cell. These velocity vectors were plotted on the Seurat UMAP. To confirm findings from RNA velocity, we next subjected our cells to pseudo-temporal ordering using Monocle 2 (ref. 96). Monocle 2 was used to identify genes that were differentially expressed over pseudo-time and organized in a self-organizing map with eight modules. Pseudo-temporal values assigned to single cells were integrated in our Seurat object, and the pseudo-temporal ordering was plotted on the UMAP. DAVID was used to perform GO analysis for the eight modules.

Bulk RNA-seq and ChIC-seq

Heart isolation was performed on whole zebrafish hearts 14 days after tamoxifen treatment, after which hearts were dissociated into single cells. For RNA-seq, fish either contained three transgenes allowing CM-specific OE of hmga1a-eGFP Tg(ubi:Loxp-stop-Loxp-hmga1a-eGFP), Tg(myl7:DsRed2-NLS) and Tg(myl7:CreER)^{pd10} or formed the control fish containing only two transgenes (Tg(myl7:DsRed2-NLS) and Tg(myl7:CreER)^{pd10}). For ChIC experiments, fish contained Tg(myl7:LiveAct-TdTomato) instead of Tg(myl7:DsRed2-NLS) because of fluorophore compatibility with the sortChIC pipeline. Use of these lines allows fluorescence-activated cell sorting (FACS) of CMs after antibody incubation.

For bulk RNA-seq, 4 × 1,000 DsRed$^+$ cells were sorted from pooled Cre-only control ($n = 14$) hearts and 4 × 1,000 DsRed$^+$ cells from pooled hmga1a–eGFP ($n = 14$) hearts. Bulk RNA-seq was performed by Single Cell Discoveries. Cells were lysed in TRIzol; RNA was extracted; and libraries were prepared and sequenced on the Illumina platform. FASTQ files were mapped with the STARandGO pipeline (https://github.com/anna-alemany/VASAseq/blob/main/mapping/map_star.sh) against the danRer11 Ensembl genome with the zebrafish Lawson V4.3.2 annotation. Normalization and downstream analysis were performed in R. Owing to low read count, 1/4 control and 1/4 OE technical replicates were excluded from analysis. Using the R package edgeR, differentially expressed genes were obtained (FC < −1 or FC > 1 and $P < 0.05$). Gene lists were subjected to GO analysis using the online tool DAVID.

Bulk sortChIC-seq was performed by Single-Cell Core (Oncode Institute). In short, for zebrafish experiments using bulk sortChIC[57], single-cell suspensions from Cre-only control ($n = 10$) and hmga1a–eGFP ($n = 10$) hearts were subjected to the sortChIC protocol and incubated with antibodies against H3K4me3 (Invitrogen, MA-5-11199, 1:400), H3K9me3 (Invitrogen, MA5-33395, 1:200) or H3K27me3 (Cell Signaling Technology, C36B11, 1:200). The next day, cells were FACS sorted based on LiveAct-TdTomato$^+$ post-antibody incubation in tubes of 100 cells. ChIC-seq libraries were subsequently prepared on sorted cells. Data pre-processing was performed using the SingleCellMultiOmics package (https://github.com/BuysDB/SingleCellMultiOmics), and the sequences were mapped to the zebrafish danRer11 Ensembl genome using Burrows–Wheeler Aligner (BWA). Data were uploaded to the Galaxy web platform, and the public server at https://usegalaxy.org/ was used to analyze the data. Reads were normalized to counts per million (CPM). Minimum mapping quality threshold was put at 50, and duplicates and quality control fails were filtered out (flag 1536) during BAM to BigWig conversion. To integrate ChIC-seq data with RNA-seq data, locations of all zebrafish genes were obtained from Ensembl BioMart, danRer11. For the mouse ChIC-seq experiment, BZ regions were manually excised from 14-dpi hearts of control mice ($n = 4$) and *Hmga1* OE mice ($n = 3$), and CM nuclei isolation was performed as described previously[30]. Single-nuclei suspensions were subjected to the sortChIC protocol and incubated with H3K27me3 antibody (Cell Signaling Technlology, 36B11, 1:200). The next day, CM nuclei were FACS sorted on GFP to select transduced CMs (1,000 cells per sample) and used for ChIC-seq library preparation. Data pre-processing was performed using the SingleCellMultiOmics package (https://github.com/BuysDB/SingleCellMultiOmics), and the sequences were mapped

to the *Mus musculus* GRC38m38.p6 Ensembl genome using BWA. Data were uploaded to the Galaxy web platform, and the public server at https://usegalaxy.org/ was used to analyze the data. Reads were normalized to CPM. Minimum mapping quality threshold was put at 50, and duplicates and quality control fails were filtered out (flag 1536) during BAM to BigWig conversion.

Statistics and reproducibility

All experiments were performed with at least three biological replicates per group and were performed twice with similar results, with some exceptions. Mouse TOMO-seq, zebrafish scRNA-seq, zebrafish/mouse ChIC-seq, mouse qPCR for *Hmga1* in neonatal samples and long-term *hmga1a* OE experiments were performed once.

All data were quantified in a double-blinded fashion. Statistical testing methods are indicated in the description of each figure. Statistical analyses were performed using GraphPad Prism (GraphPad Software). Histological quantifications of CM proliferation in zebrafish were performed using Imaris 64 (version 3.2.1) software (Oxford Instruments) and were performed either in the BZ, which was defined as 200 µm from the wound border, or throughout the ventricle for uninjured contexts, in both cases on three sections per heart, of at least three hearts. Quantifications of scar size on AFOG-stained zebrafish hearts were performed by staining all sections of each heart and measuring the remaining scar area in ImageJ software (National Institutes of Health). pS6 signal in zebrafish hearts was quantified using both Imaris 64 (version 3.2.1) software tools to mask tropomyosin and obtain CM-specific pS6 signal and ImageJ software to measure the intensity and area of the $pS6^+$/$tropomyosin^+$ area in the BZ (300 µm). H3K27me3 staining was quantified for both zebrafish and mouse sections using ImageJ software to measure signal intensity in individual nuclei. Quantification of cell size using WGA staining was performed using ImageJ to measure the surface area of transversely cut CMs. Quantification of CM proliferation in NRVMs was performed using Imaris 64 (version 3.2.1) software, counting every CM across three slides per condition, representing biological replicates. CM proliferation in mouse heart sections was performed using Imaris 64 (version 3.2.1) software, where the BZ was defined as 500 µm from the wound border, and at least three squares of 500 µm × 500 µm were selected for quantification in the BZ and one for quantification in the RZ. Analysis of echocardiography in the mouse was performed using Vevo software to measure the end-diastolic volume and the end-systolic volume, using Simpson's method. Quantification of scar size on mouse heart sections at 42 dpi was performed using ImageJ software to obtain a midline length measurement readout (% MI midline of total LV midline[97]).

Reporting summary

Further information on research design is available in the Nature Portfolio Reporting Summary linked to this article.

Data availability

The data presented are available in the main text, figures, extended data figures or the supplementary materials. Source data are provided with this publication. Sequencing data can be found in the Gene Expression Omnibus under accession number GSE241159. Mouse TOMO-seq data can also be viewed and searched at http://mouse.genomes.nl/tomo-seq/2018/. Other information is available from the corresponding author upon reasonable request.

Code availability

All code used in the paper is from freely accessible R packages. The package edgeR was used for differential gene expression analyses. Genome coverage data from ChIC-seq experiments were analyzed using the Galaxy platform (https://usegalaxy.org/). Details are provided in figure legends and the Methods section.

References

1. Patterson, M. et al. Frequency of mononuclear diploid cardiomyocytes underlies natural variation in heart regeneration. *Nat. Genet.* **49**, 1346–1353 (2017).
2. Gonzalez-Rosa, J. M. et al. Myocardial polyploidization creates a barrier to heart regeneration in zebrafish. *Dev. Cell* **44**, 433–446 (2018).
3. Windmueller, R. et al. Direct comparison of mononucleated and binucleated cardiomyocytes reveals molecular mechanisms underlying distinct proliferative competencies. *Cell Rep.* **30**, 3105–3116 (2020).
4. Puente, B. N. et al. The oxygen-rich postnatal environment induces cardiomyocyte cell-cycle arrest through DNA damage response. *Cell* **157**, 565–579 (2014).
5. Honkoop, H. et al. Single-cell analysis uncovers that metabolic reprogramming by ErbB2 signaling is essential for cardiomyocyte proliferation in the regenerating heart. *eLife* **8**, e50163 (2019).
6. Bae, J. et al. Malonate promotes adult cardiomyocyte proliferation and heart regeneration. *Circulation* **143**, 1973–1986 (2021).
7. Magadum, A. et al. Pkm2 regulates cardiomyocyte cell cycle and promotes cardiac regeneration. *Circulation* **141**, 1249–1265 (2020).
8. Porrello, E. R. et al. Transient regenerative potential of the neonatal mouse heart. *Science* **331**, 1078–1080 (2011).
9. Heallen, T. et al. Hippo signaling impedes adult heart regeneration. *Development* **140**, 4683–4690 (2013).
10. Leach, J. P. et al. Hippo pathway deficiency reverses systolic heart failure after infarction. *Nature* **550**, 260–264 (2017).
11. D'Uva, G. et al. ERBB2 triggers mammalian heart regeneration by promoting cardiomyocyte dedifferentiation and proliferation. *Nat. Cell Biol.* **17**, 627–638 (2015).
12. Lesizza, P. et al. Single-dose intracardiac injection of pro-regenerative microRNAs improves cardiac function after myocardial infarction. *Circ. Res.* **120**, 1298–1304 (2017).
13. Aharonov, A. et al. ERBB2 drives YAP activation and EMT-like processes during cardiac regeneration. *Nat. Cell Biol.* **22**, 1346–1356 (2020).
14. Monroe, T. O. et al. YAP partially reprograms chromatin accessibility to directly induce adult cardiogenesis in vivo. *Dev. Cell* **48**, 765–779 (2019).
15. Xin, M. et al. Hippo pathway effector Yap promotes cardiac regeneration. *Proc. Natl Acad. Sci. USA* **110**, 13839–13844 (2013).
16. Shakked, A. et al. Redifferentiated cardiomyocytes retain residual dedifferentiation signatures and are protected against ischemic injury. *Nat. Cardiovasc. Res.* **2**, 383–398 (2023).
17. Gabisonia, K. et al. MicroRNA therapy stimulates uncontrolled cardiac repair after myocardial infarction in pigs. *Nature* **569**, 418–422 (2019).
18. Yan, R. et al. An enhancer-based gene-therapy strategy for spatiotemporal control of cargoes during tissue repair. *Cell Stem Cell* **30**, 96–111(2023).
19. Poss, K. D., Wilson, L. G. & Keating, M. T. Heart regeneration in zebrafish. *Science* **298**, 2188–2190 (2002).
20. Goldman, J. A. et al. Resolving heart regeneration by replacement histone profiling. *Dev. Cell* **40**, 392–404 (2017).
21. Ogawa, M. et al. Krüppel-like factor 1 is a core cardiomyogenic trigger in zebrafish. *Science* **372**, 201–205 (2021).
22. Jopling, C. et al. Zebrafish heart regeneration occurs by cardiomyocyte dedifferentiation and proliferation. *Nature* **464**, 606–609 (2010).
23. Kikuchi, K. et al. Primary contribution to zebrafish heart regeneration by $gata4^+$ cardiomyocytes. *Nature* **464**, 601–605 (2010).
24. Wu, C. C. et al. Spatially resolved genome-wide transcriptional profiling identifies BMP signaling as essential regulator of zebrafish cardiomyocyte regeneration. *Dev. Cell* **36**, 36–49 (2016).

25. Beisaw, A. et al. AP-1 contributes to chromatin accessibility to promote sarcomere disassembly and cardiomyocyte protrusion during zebrafish heart regeneration. *Circ. Res.* **126**, 1760–1778 (2020).
26. Nguyen, P. D. et al. Interplay between calcium and sarcomeres directs cardiomyocyte maturation during regeneration. *Science* **380**, 758–764 (2023).
27. Sharov, V. G. et al. Abnormalities of cardiocytes in regions bordering fibrous scars of dogs with heart failure. *Int. J. Cardiol.* **60**, 273–279 (1997).
28. Dispersyn, G. D. et al. Dissociation of cardiomyocyte apoptosis and dedifferentiation in infarct border zones. *Eur. Heart J.* **23**, 849–857 (2002).
29. Ursell, P. C., Gardner, P. I., Albala, A., Fenoglio, J. J. J. & Wit, A. L. Structural and electrophysiological changes in the epicardial border zone of canine myocardial infarcts during infarct healing. *Circ. Res.* **56**, 436–451 (1985).
30. van Duijvenboden, K. et al. Conserved *NPPB*$^{+}$ border zone switches from MEF2- to AP-1-driven gene program. *Circulation* **140**, 864–879 (2019).
31. Wang, Y. et al. Genetic basis of ruminant headgear and rapid antler regeneration. *Science* **364**, eaav6335 (2019).
32. Sinha, S. et al. Fibroblast inflammatory priming determines regenerative versus fibrotic skin repair in reindeer. *Cell* **185**, 4717–4736 (2022).
33. Lai, S. L. et al. Reciprocal analyses in zebrafish and medaka reveal that harnessing the immune response promotes cardiac regeneration. *eLife* **6**, e25605 (2017).
34. Stockdale, W. T. et al. Heart regeneration in the Mexican cavefish. *Cell Rep.* **25**, 1997–2007 (2018).
35. Pasumarthi, K. B., Nakajima, H., Nakajima, H. O., Soonpaa, M. H. & Field, L. J. Targeted expression of cyclin D2 results in cardiomyocyte DNA synthesis and infarct regression in transgenic mice. *Circ. Res.* **96**, 110–118 (2005).
36. Junker, J. P. et al. Genome-wide RNA tomography in the zebrafish embryo. *Cell* **159**, 662–675 (2014).
37. Sergeeva, I. A. et al. A transgenic mouse model for the simultaneous monitoring of ANF and BNP gene activity during heart development and disease. *Cardiovasc. Res.* **101**, 78–86 (2014).
38. Nakada, Y. et al. Hypoxia induces heart regeneration in adult mice. *Nature* **541**, 222–227 (2017).
39. Kuppe, C. et al. Spatial multi-omic map of human myocardial infarction. *Nature* **608**, 766–777 (2022).
40. Lepilina, A. et al. A dynamic epicardial injury response supports progenitor cell activity during zebrafish heart regeneration. *Cell* **127**, 607–619 (2006).
41. Fukuda, R. et al. Stimulation of glycolysis promotes cardiomyocyte proliferation after injury in adult zebrafish. *EMBO Rep.* **21**, e49752 (2020).
42. Reeves, R. HMGA proteins: flexibility finds a nuclear niche? *Biochem. Cell Biol.* **81**, 185–195 (2003).
43. Battista, S. et al. Loss of *Hmga1* gene function affects embryonic stem cell lympho-hematopoietic differentiation. *FASEB J.* **17**, 1496–1498 (2003).
44. Kishi, Y., Fujii, Y., Hirabayashi, Y. & Gotoh, Y. HMGA regulates the global chromatin state and neurogenic potential in neocortical precursor cells. *Nat. Neurosci.* **15**, 1127–1133 (2012).
45. Shah, S. N. et al. HMGA1 reprograms somatic cells into pluripotent stem cells by inducing stem cell transcriptional networks. *PLoS ONE* **7**, e48533 (2012).
46. Xian, L. et al. HMGA1 amplifies Wnt signalling and expands the intestinal stem cell compartment and Paneth cell niche. *Nat. Commun.* **8**, 15008 (2017).
47. Willcockson, M. A. et al. H1 histones control the epigenetic landscape by local chromatin compaction. *Nature* **589**, 293–298 (2021).
48. Yusufova, N. et al. Histone H1 loss drives lymphoma by disrupting 3D chromatin architecture. *Nature* **589**, 299–305 (2021).
49. La Manno, G. et al. RNA velocity of single cells. *Nature* **560**, 494–498 (2018).
50. Stonyte, V., Boye, E. & Grallert, B. Regulation of global translation during the cell cycle. *J. Cell Sci.* **131**, jcs220327 (2018).
51. Montemurro, C. et al. Cell cycle-related metabolism and mitochondrial dynamics in a replication-competent pancreatic beta-cell line. *Cell Cycle* **16**, 2086–2099 (2017).
52. Gemberling, M., Karra, R., Dickson, A. L. & Poss, K. D. Nrg1 is an injury-induced cardiomyocyte mitogen for the endogenous heart regeneration program in zebrafish. *eLife* **4**, e05871 (2015).
53. Roux, P. P. et al. RAS/ERK signaling promotes site-specific ribosomal protein S6 phosphorylation via RSK and stimulates cap-dependent translation. *J. Biol. Chem.* **282**, 14056–14064 (2007).
54. Calcagno, D. M. et al. Single-cell and spatial transcriptomics of the infarcted heart define the dynamic onset of the border zone in response to mechanical destabilization. *Nat. Cardiovasc. Res.* **1**, 1039–1055 (2022).
55. Catez, F. et al. Network of dynamic interactions between histone H1 and high-mobility-group proteins in chromatin. *Mol. Cell. Biol.* **24**, 4321–4328 (2004).
56. Zhao, K., Kas, E., Gonzalez, E. & Laemmli, U. K. SAR-dependent mobilization of histone H1 by HMG-I/Y in vitro: HMG-I/Y is enriched in H1-depleted chromatin. *EMBO J.* **12**, 3237–3247 (1993).
57. Zeller, P. et al. Single-cell sortChIC identifies hierarchical chromatin dynamics during hematopoiesis. *Nat. Genet.* **55**, 333–345 (2023).
58. Tzahor, E. & Poss, K. D. Cardiac regeneration strategies: staying young at heart. *Science* **356**, 1035–1039 (2017).
59. Zhu, W. et al. Regenerative potential of neonatal porcine hearts. *Circulation* **138**, 2809–2816 (2018).
60. Lin, Z. et al. Cardiac-specific YAP activation improves cardiac function and survival in an experimental murine MI model. *Circ. Res.* **115**, 354–363 (2014).
61. Xiang, F. L., Guo, M. & Yutzey, K. E. Overexpression of Tbx20 in adult cardiomyocytes promotes proliferation and improves cardiac function after myocardial infarction. *Circulation* **133**, 1081–1092 (2016).
62. Aurora, A. B. et al. Macrophages are required for neonatal heart regeneration. *J. Clin. Invest.* **124**, 1382–1392 (2014).
63. Wu, Q. Q. et al. High-mobility group AT-hook 1 promotes cardiac dysfunction in diabetic cardiomyopathy via autophagy inhibition. *Cell Death Dis.* **11**, 160 (2020).
64. Jagannathan, M., Cummings, R. & Yamashita, Y. M. A conserved function for pericentromeric satellite DNA. *eLife* **7**, e34122 (2018).
65. Reeves, R. Nuclear functions of the HMG proteins. *Biochim. Biophys. Acta* **1799**, 3–14 (2010).
66. Olan, I. et al. HMGA1 orchestrates chromatin compartmentalization and sequesters genes into 3D networks coordinating senescence heterogeneity. *Nat. Commun.* **15**, 6891 (2024).
67. Ozturk, N., Singh, I., Mehta, A., Braun, T. & Barreto, G. HMGA proteins as modulators of chromatin structure during transcriptional activation. *Front. Cell Dev. Biol.* **2**, 5 (2014).
68. Narita, M. et al. A novel role for high-mobility group a proteins in cellular senescence and heterochromatin formation. *Cell* **126**, 503–514 (2006).
69. Teano, G. et al. Histone H1 protects telomeric repeats from H3K27me3 invasion in *Arabidopsis*. *Cell Rep.* **42**, 112894 (2022).
70. Rutowicz, K. et al. Linker histones are fine-scale chromatin architects modulating developmental decisions in *Arabidopsis*. *Genome Biol.* **20**, 157 (2019).

71. Vastenhouw, N. L. & Schier, A. F. Bivalent histone modifications in early embryogenesis. *Curr. Opin. Cell Biol.* **24**, 374–386 (2012).
72. Boyer, L. A. et al. Polycomb complexes repress developmental regulators in murine embryonic stem cells. *Nature* **441**, 349–353 (2006).
73. Munshi, N. et al. Coordination of a transcriptional switch by HMGI(Y) acetylation. *Science* **293**, 1133–1136 (2001).
74. Banks, G. C., Li, Y. & Reeves, R. Differential in vivo modifications of the HMGI(Y) nonhistone chromatin proteins modulate nucleosome and DNA interactions. *Biochemistry* **39**, 8333–8346 (2000).
75. Xu, M. et al. Core promoter-selective function of HMGA1 and mediator in initiator-dependent transcription. *Genes Dev.* **25**, 2513–2524 (2011).
76. Li, R. G. et al. YAP induces a neonatal-like pro-renewal niche in the adult heart. *Nat. Cardiovasc. Res.* **3**, 283–300 (2024).
77. Ninh, V. K. et al. Spatially clustered type I interferon responses at injury borderzones. *Nature* **633**, 174–181 (2024).
78. Huang, D. W., Sherman, B. T. & Lempicki, R. A. Systematic and integrative analysis of large gene lists using DAVID. *Nat. Protoc.* **4**, 44–57 (2009).
79. Mably, J. D., Mohideen, M. A., Burns, C. G., Chen, J. N. & Fishman, M. C. *heart of glass* regulates the concentric growth of the heart in zebrafish. *Curr. Biol.* **13**, 2138–2147 (2003).
80. Kwan, K. M. et al. The Tol2kit: a multisite gateway-based construction kit for *Tol2* transposon transgenesis constructs. *Dev. Dyn.* **236**, 3088–3099 (2007).
81. Mosimann, C. et al. Ubiquitous transgene expression and Cre-based recombination driven by the *ubiquitin* promoter in zebrafish. *Development* **138**, 169–177 (2011).
82. Schnabel, K., Wu, C. C., Kurth, T. & Weidinger, G. Regeneration of cryoinjury induced necrotic heart lesions in zebrafish is associated with epicardial activation and cardiomyocyte proliferation. *PLoS ONE* **6**, e18503 (2011).
83. Gladka, M. M. et al. Cardiomyocytes stimulate angiogenesis after ischemic injury in a ZEB2-dependent manner. *Nat. Commun.* **12**, 84 (2021).
84. Arsic, N. et al. Vascular endothelial growth factor stimulates skeletal muscle regeneration in vivo. *Mol. Ther.* **10**, 844–854 (2004).
85. Inagaki, K., Storm, T. A., Kay, M. A. & Nakai, H. 5. Mechanisms for hairpin loop opening of 'closed' AAV-ITRs by specific cellular endonuclease activities, a prerequisite for rAAV vector genome recombinations in vivo. *Mol. Ther.* **13**, S2–S3 (2006).
86. Ayuso, E. et al. High AAV vector purity results in serotype- and tissue-independent enhancement of transduction efficiency. *Gene Ther.* **17**, 503–510 (2010).
87. Zentilin, L., Marcello, A. & Giacca, M. Involvement of cellular double-stranded DNA break binding proteins in processing of the recombinant adeno-associated virus genome. *J. Virol.* **75**, 12279–12287 (2001).
88. Kinkel, M. D., Eames, S. C., Philipson, L. H. & Prince, V. E. Intraperitoneal injection into adult zebrafish. *J. Vis. Exp.* **30**, 2126 (2010).
89. Honkoop, H., Nguyen, P. D., van der Velden, V. E. M., Sonnen, K. F. & Bakkers, J. Live imaging of adult zebrafish cardiomyocyte proliferation ex vivo. *Development* **148**, dev199740 (2021).
90. Moorman, A. F., Houweling, A. C., de Boer, P. A. & Christoffels, V. M. Sensitive nonradioactive detection of mRNA in tissue sections: novel application of the whole-mount in situ hybridization protocol: novel application of the whole-mount in situ hybridization protocol. *J. Histochem. Cytochem.* **49**, 1–8 (2001).
91. Robinson, M. D., McCarthy, D. J. & Smyth, G. K. edgeR: a Bioconductor package for differential expression analysis of digital gene expression data. *Bioinformatics* **26**, 139–140 (2010).
92. Muraro, M. J. et al. A single-cell transcriptome atlas of the human pancreas. *Cell Syst.* **3**, 385–394 (2016).
93. Hashimshony, T. et al. CEL-Seq2: sensitive highly-multiplexed single-cell RNA-Seq. *Genome Biol.* **17**, 77 (2016).
94. Hao, Y. et al. Integrated analysis of multimodal single-cell data. *Cell* **184**, 3573–3587 (2021).
95. Dobin, A. et al. STAR: ultrafast universal RNA-seq aligner. *Bioinformatics* **29**, 15–21 (2013).
96. Trapnell, C. et al. The dynamics and regulators of cell fate decisions are revealed by pseudotemporal ordering of single cells. *Nat. Biotechnol.* **32**, 381–386 (2014).
97. Nascimento, D. S. et al. MIQuant—semi-automation of infarct size assessment in models of cardiac ischemic injury. *PLoS ONE* **6**, e25045 (2011).

Acknowledgements

We thank the Hubrecht Imaging Center, the Hubrecht Animal Facility and the Oncode Single Cell Core for technical assistance; H. Begthel and J. Korving for histology assistance; A. Griffa and H. van Beijnum for consulting on bioinformatic analysis; A. Cardona for providing mouse heart protein lysates for western blot; C. Bart and A. de Vries for preparation of the AAV9Myo4a packaging plasmid; and I. Gooijers, L. Florit Gonzalez and F. Tessadori for their input on the paper.
This work was supported by the Netherlands Cardiovascular Initiative with support from the Netherlands Heart Foundation and Hartekind (CVON2019-2 OUTREACH and 2013T091 COBRA3) (D.E.M.d.B., M.B., R.J., I.B.H., M. Günthel, V.M.C. and J.B.). It was also supported by the following:
ERA-CVD Grant (JCT2016-40-0) (H.H. and J.B.)
EMBO Long-Term Fellowship (ALTF1129-2015) (P.D.N.)
HFSPO Fellowship (LT001404/2017-L) (P.D.N.)
NWO-ZonMW Veni Grant (016.186.017-3) (P.D.N.)
EIC Transition Grant (TRACTION) (G.J.J.B. and V.M.C.)

Author contributions

Conceptualization: M.B., D.E.M.d.B. and J.B. Investigation: M.B., D.E.M.d.B., H.H., A.E.G., D.V., A.R.B., P.D.N., M.S., D.C., M.V.-G., L.K., R.J., I.B.H., M. Günthel, K.J.V., M.K. and L.Z. Supervision: M. Giacca, J.K., E.v.R., G.J.J.B., V.M.C. and J.B. Funding acquisition: M. Giacca, J.K., G.J.J.B., E.v.R., V.M.C. and J.B. Writing—original draft: D.E.M.d.B., M.B. and J.B. Writing—review and editing: all authors.

Competing interests

D.E.M.d.B. and J.B. are co-inventors on a patent application associated with this study: patent no. PCT/NL2022/050553, 'Mammalian heart regeneration'. J.B. is co-founder of Myogene Therapeutics. The other authors declare no competing interests.

Additional information

Extended data is available for this paper at https://doi.org/10.1038/s44161-024-00588-9.

Supplementary information The online version contains supplementary material available at https://doi.org/10.1038/s44161-024-00588-9.

Correspondence and requests for materials should be addressed to Jeroen Bakkers.

Peer review information *Nature Cardiovascular Research* thanks Ching-Ling Lien and the other, anonymous, reviewer(s) for their contribution to the peer review of this work.

[1]Hubrecht Institute, Royal Netherlands Academy of Arts and Sciences (KNAW) and University Medical Center Utrecht, Utrecht, The Netherlands. [2]Department of Medical Biology, Amsterdam Cardiovascular Sciences, Amsterdam University Medical Centers, Amsterdam, The Netherlands. [3]PacingCure BV, Amsterdam, The Netherlands. [4]Australian Regenerative Medicine Institute, Monash University, Melbourne, VIC, Australia. [5]International Centre for Genetic Engineering and Biotechnology (ICGEB), University of Trieste, Trieste, Italy. [6]School of Cardiovascular and Metabolic Medicine and Sciences, King's College London, London, UK. [7]Department of Cardiology, Amsterdam Cardiovascular Sciences, Amsterdam University Medical Centers, Amsterdam, The Netherlands. [8]Department of Cardiology, Division of Heart and Lungs, University Medical Center Utrecht, Utrecht, The Netherlands. [9]Department of Pediatric Cardiology, Division of Pediatrics, University Medical Center Utrecht, Utrecht, The Netherlands. [10]Present address: Leibniz Institute on Aging, Fritz Lipmann Institute (FLI), Jena, Germany. [11]Present address: Institut Curie, Université PSL, CNRS UMR3215, INSERM U934, Paris, France. [12]These authors contributed equally: Mara Bouwman, Dennis E. M. de Bakker. ✉e-mail: j.bakkers@hubrecht.eu

https://doi.org/10.1038/s44161-024-00588-9

A

Representative GOs	Pval.
Extracellular exosome	4.77E-18
Glycoprotein	6.94E-17
Extracellular matrix	7.74E-13
Phosphoprotein	1.07E-12
Endoplasmic reticulum	3.29E-10
Collagen	1.79E-09
Secreted	8.62E-09
Focal adhesion	9.72E-09
Cell migration	8.84E-08
Calcium	3.91E-07

B

Representative GOs	Pval.
Mitochondrion	1.27E-120
Transit peptide	1.41E-99
Oxidative phosphorylation	2.49E-42
Metabolic pathways	9.22E-42
Respiratory chain	1.40E-34
Acetylation	1.81E-24
Ubiquinone	1.14E-16
NAD binding	1.55E-12
Z disc	5.30E-11
Lipid metabolism	3.10E-09

C

Representative GOs	Pval.
Phosphoprotein	1.36E-30
Acetylation	6.04E-15
Extracellular exosome	3.94E-05
Cytoskeleton	1.27E-03
Protein biosynthesis	2.67E-03
Myofibril	4.62E-03
Heart development	7.48E-03
Regulation of proliferation	7.85E-03
Spindle	1.43E-02
Actin binding	4.46E-02

D

Representative GOs	Pval.
Phosphoprotein	5.01E-10
Alternative splicing	8.41E-07
Extracellular exosome	1.04E-05
Disulfide bond	3.22E-05
Glycoprotein	4.33E-05
Cell growth	1.92E-04
Cell projection	5.00E-04
Extracellular matrix	5.21E-04
Response to hypoxia	6.41E-03
TGF-beta signaling	1.34E-02

E

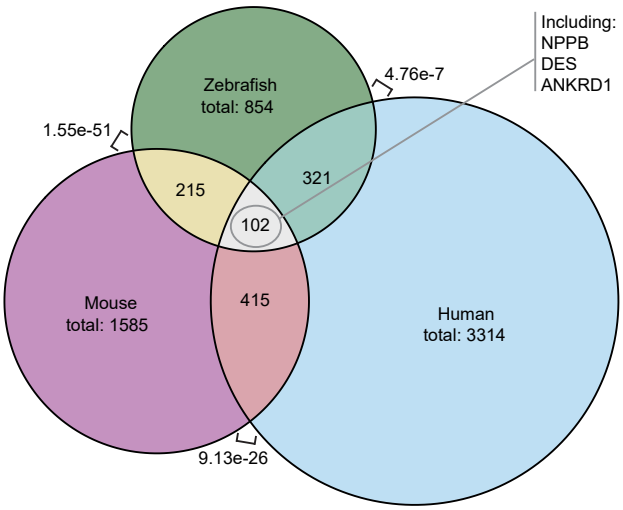

F

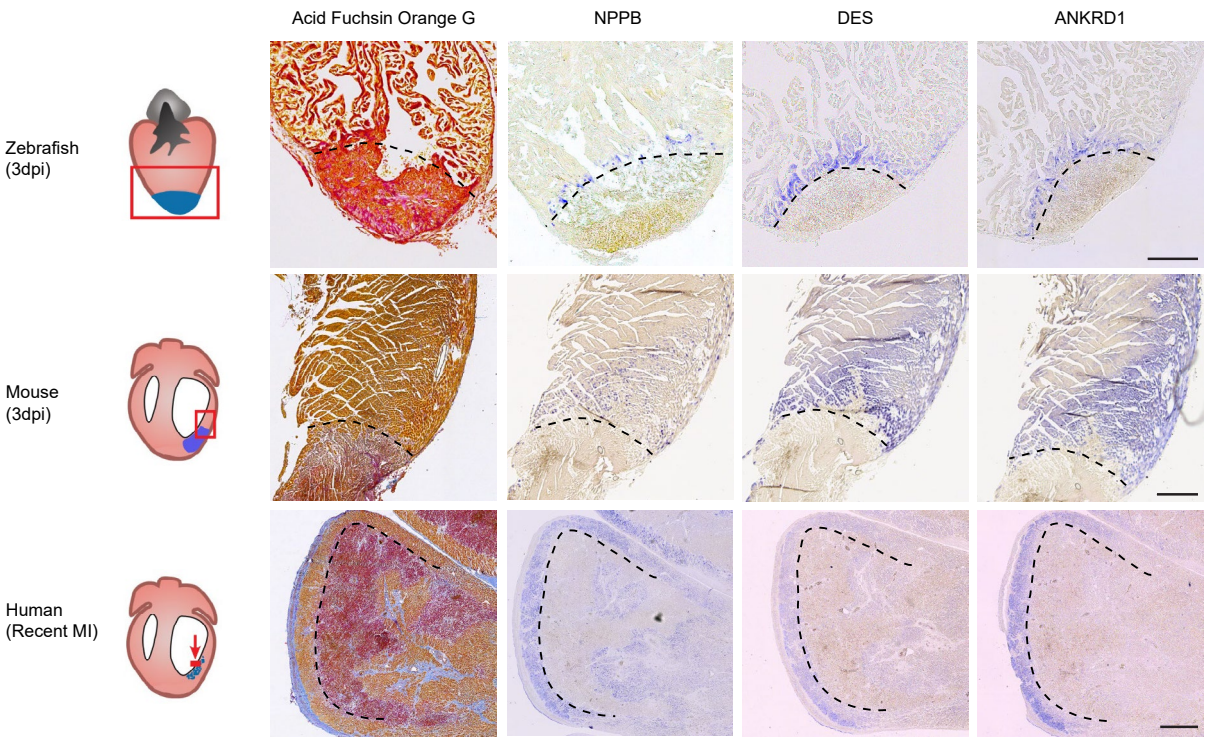

Extended Data Fig. 1 | See next page for caption.

https://doi.org/10.1038/s44161-024-00588-9

Extended Data Fig. 1 | Interspecies comparison of BZ transcriptional profiles. (**a-d**) Gene ontologies on BZ transcriptomes shown in Fig. 2b. P-values obtained with DAVID online GO analysis which uses the EASE score, a modified fishers exact p-value[78]. (**e**) Venn diagram displaying the overlap between genes overexpressed ($p < 0.01$) in the BZ of the mouse and zebrafish, as defined by the TOMO-seq analysis, as well as with human BZ genes characterized by Kuppe et al.[39], using genes identified in at least two out of three BZ gene lists created (dataset IDs: AKK003_157777, AKK002_157781, AKK001_157785). Human and zebrafish gene names were translated to mouse gene names prior to the intersect analysis. Overlap significance was calculated using the R package Phyper to run a hypergeometric test, showing significance between zebrafish and mouse ($p = 1.55e\text{-}51$), zebrafish and human ($p = 4.76e\text{-}7$ and mouse with human ($p = 9.13e\text{-}26$). (**f**) Histological validation of BZ genes shared between zebrafish, mouse and humans, using *in situ* hybridization. n = 3 hearts were analyzed per zebrafish and mouse staining, n = 1 for human. Results for mouse and human BZ genes were described previously[30]. Scale bars represent 100µm in zebrafish heart images, 500µm in mouse heart images and 1000µm in human heart images.

https://doi.org/10.1038/s44161-024-00588-9

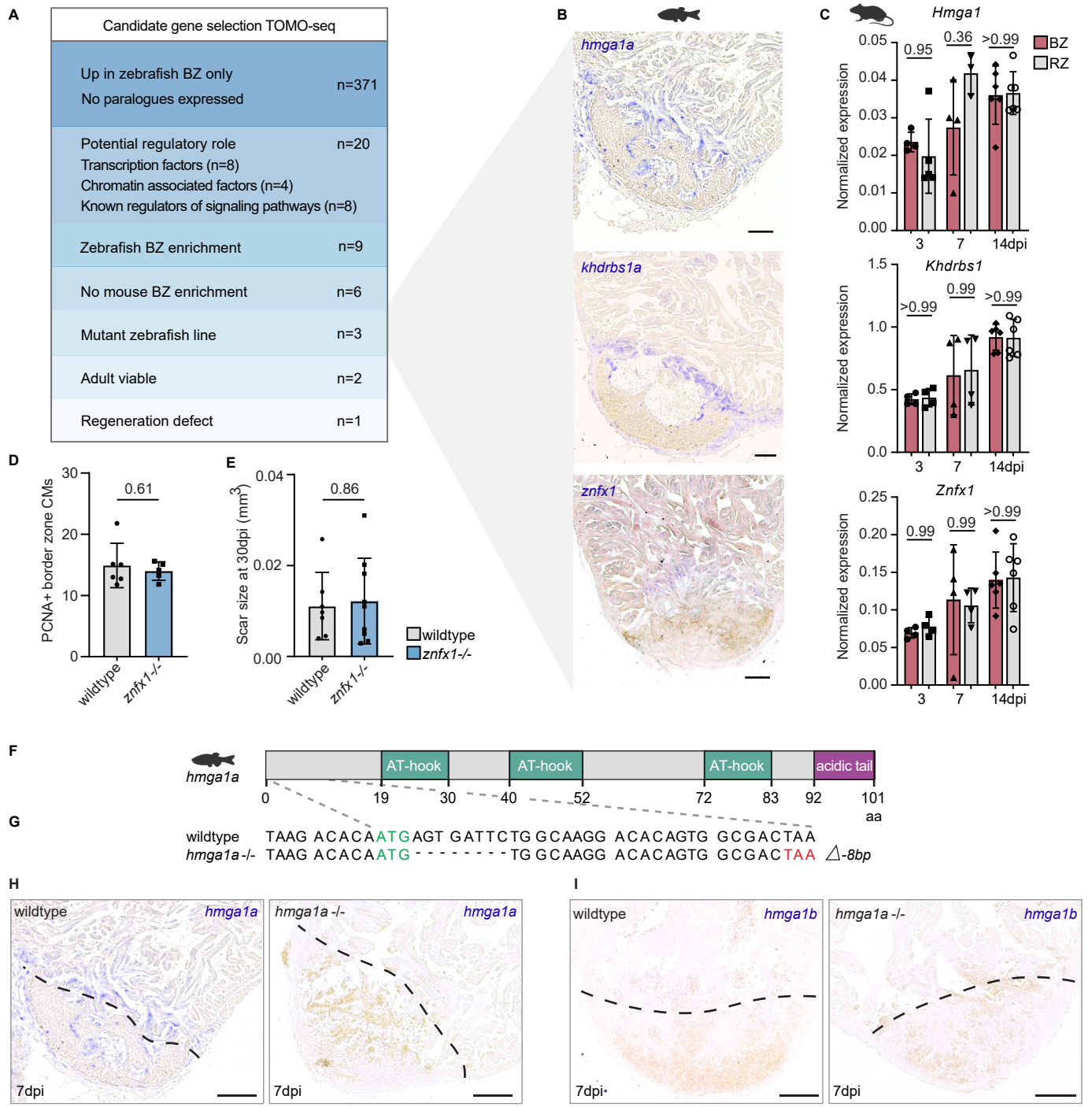

Extended Data Fig. 2 | Candidate gene selection and generation of the *hmga1a* mutant line. (**a**) Overview of candidate gene selection starting with TOMO-seq identified zebrafish specific border zone genes. (**b**) Representative images of *in situ* hybridization on 7dpi zebrafish hearts against the remaining three candidate genes: *hmga1a, khdrbs1a* and *znfx1*. n = 3 hearts were analysed per staining. Scale bars represent 50µm. (**c**) Normalized expression for *Hmga1, Khdrbs1* and *Znfx1* obtained by quantitative PCR on cDNA libraries from isolated border zone (BZ) and remote myocardial (RZ) tissue of injured mouse hearts 3 (n = 4), 7 (n = 4) or 14 (n = 6) days post MI. Gene expression was corrected for the geomean of reference genes *Hprt* and *Eefe1e* expression from the same sample. Datapoints indicate individual hearts. Error bars indicate mean ± SD. Statistics were performed using two-way ANOVA followed by Tukey's multiple comparisons test. No differences between the BZ and RZ at 3, 7 or 14dpi was observed for *Hmga1* ($p = 0.95$, $p = 0.36$, $p > 0.99$), *Khdrbs1* ($p > 0.99$, $p = 0.99$, $p > 0.99$) and *Znfx1* ($p = 0.99$, $p = 0.99$, $p > 0.99$). (**d**) Quantification of proliferating border zone cardiomyocytes based on immunofluorescent staining of Mef2 and PCNA on wildtype (n = 6) and *znfx1-/-* (n = 5) hearts at 7dpi. Datapoints represent individual hearts. Error bars indicate mean ± SD. Statistics were performed by two-tailed unpaired t-test and shows no significant difference ($p = 0.61$). (**e**) Quantification of scar size based on AFOG staining on wildtype (n = 7) and *znfx1-/-* (n = 9) hearts at 30dpi. Datapoints represent individual hearts. Error bars indicate mean ± SD. Statistics were performed by two-tailed unpaired t-test and shows no significant difference ($p = 0.86$). (**f**) Hmga1a protein structure, including 3 AT-hook DNA binding domains and a C-terminal acidic tail. (**g**) *hmga1a-/-* zebrafish were generated using a TALEN-based -8bp deletion behind the start codon (green) causing a frameshift leading to an early stop codon (red). (**h, i**) Representative images of *in situ* hybridization against (**h**) *hmga1a* or (**i**) *hmga1b* in wildtype or *hmga1a-/-* hearts. n = 3 hearts were analysed per condition. Dashed line indicates the injury border. Scale bars represent 100µm.

https://doi.org/10.1038/s44161-024-00588-9

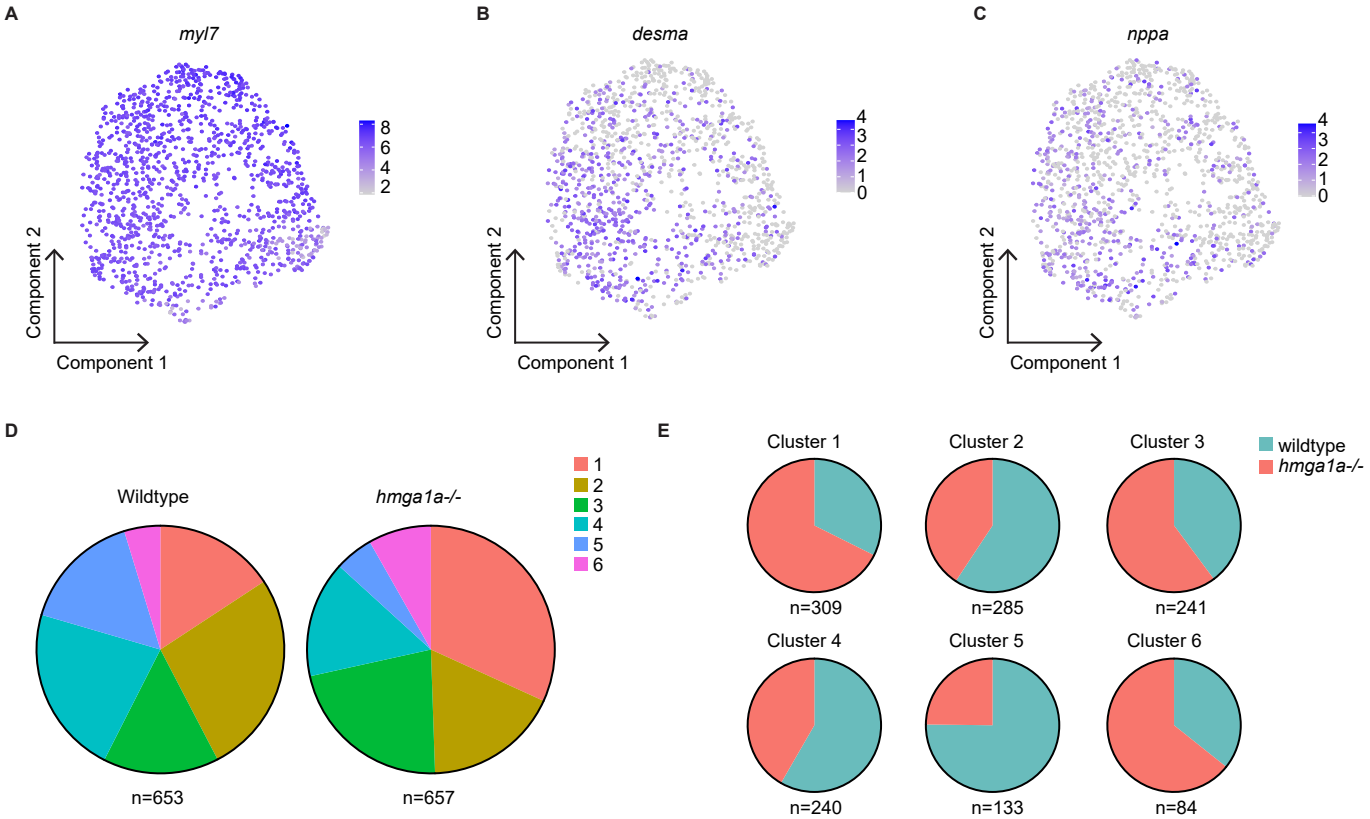

Extended Data Fig. 3 | scRNA-seq on 7dpi border zone cardiomyocytes from wildtype and *hmga1a-/-* shows heterogeneous genotype distribution over clusters. (**a-c**) UMAP representation of Log2 transformed read counts for the cardiomyocyte gene *myl7* (**a**), border zone gene *desma* (**b**) and border zone gene *nppa* (**c**). (**d**) Contribution of Seurat clusters to genotype represented as a percentage of the whole. Total number of cells per group are indicated below pie chart. (**e**) Contribution of wildtype and *hmga1a-/-* cells to the individual Seurat clusters. Total number of cells per group are indicated below pie chart.

https://doi.org/10.1038/s44161-024-00588-9

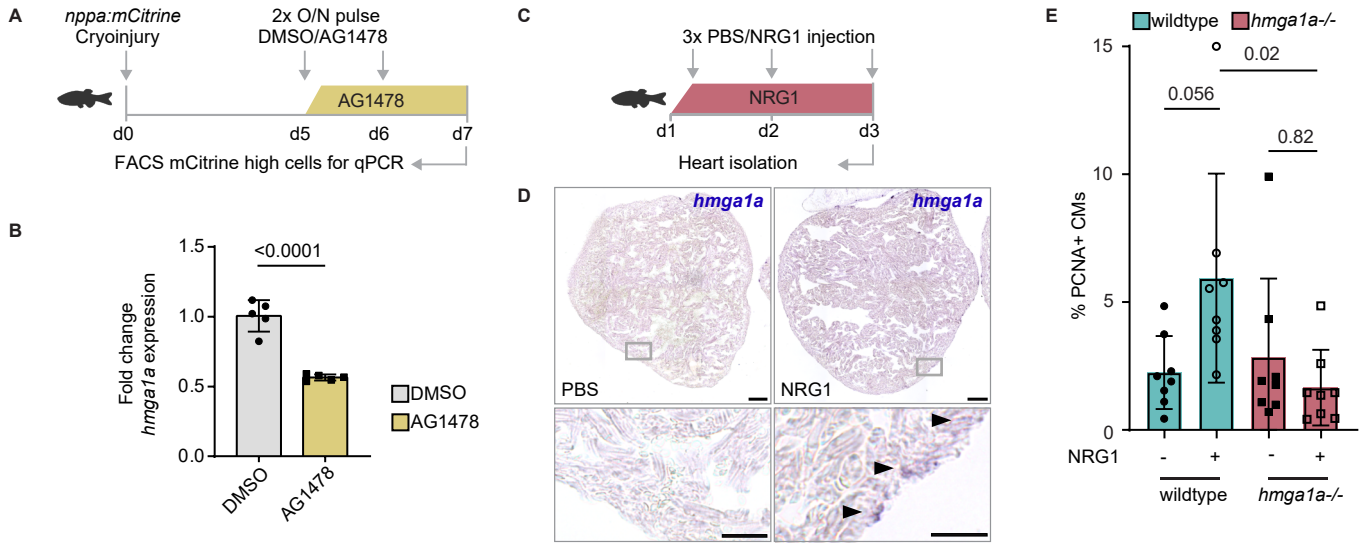

Extended Data Fig. 4 | *hmga1a* acts downstream of Nrg1/ErbB2 signaling to promote CM proliferation. (**a**) Schematic of workflow for results in (B). (**b**) Quantitative PCR analysis for *hmga1a* expression in border zone CMs treated with the ErbB2 inhibitor AG1478 or DMSO. Normalization was performed using reference gene *eef1g*. Datapoints represent technical replicates of pooled hearts (n = 5). Error bars indicate mean ± SD. Statistics were performed using a two-tailed unpaired t-test and show a significant difference ($p < 0.0001$). (**c**) Schematic of workflow for panels D and E. (**d**) Representative image of *in situ* hybridization against *hmga1a* in hearts of PBS or NRG1 injected zebrafish. Per condition, n = 6 hearts were analysed. Arrowheads indicate *hmga1a* expressing cardiomyocytes. Overview scale bars represent 100µm, zoom-in scale bars 20µm. (**e**) Quantification of proliferating cardiomyocytes based on immunofluorescent staining of Mef2 and PCNA in the ventricle of PBS (-) or NRG1 (+) injected zebrafish hearts, either in *hmga1a-/-* (n = 8 PBS, n = 8 NRG1) or wildtype sibling (n = 8 PBS, n = 8 NRG1) hearts. Data points represent individual hearts. Error bars indicate mean ± SD. Statistics were performed using a one-way ANOVA followed by Tukey's multiple comparisons test and show a near significant difference between wildtype NRG1- and NRG1+ ($p = 0.056$), a significant difference between wildtype NRG1+ and *hmga1a-/-* NRG1+ ($p = 0.02$), and no significant difference between *hmga1a-/-* NRG1- and NRG1+ ($p = 0.82$).

https://doi.org/10.1038/s44161-024-00588-9

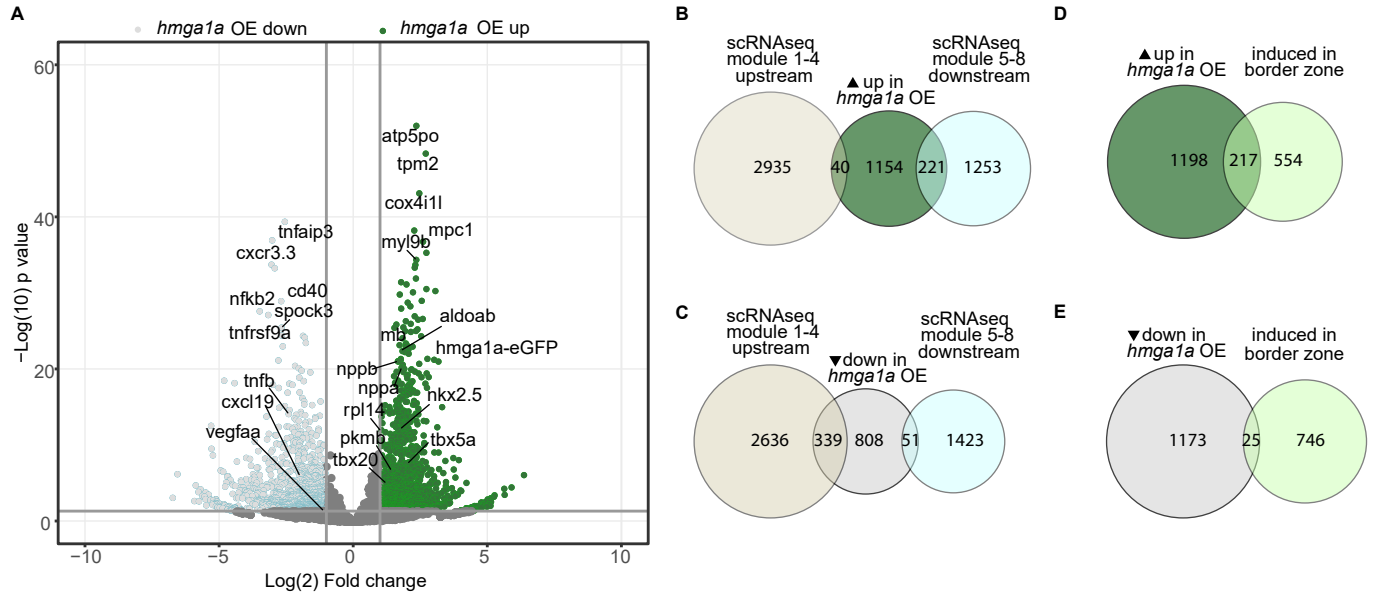

Extended Data Fig. 5 | RNA-seq reveals hmga1a OE induces a BZ-like gene expression program in cardiomyocytes. (**a**) Volcano plot showing differential gene expression analysis based on RNA-seq of pooled 14dpT control (CMs from n = 14 hearts) and *hmga1a* OE (from n = 14 hearts) CMs. Grey bars indicate cut offs at Pval <0.05 and LogFC >1 / LogFC <1. Statistics were obtained using the R package EdgeR, which uses generalized linear models (GLMs) and empirical Bayes methods to identify differentially expressed genes.(**b,c**) Venn diagrams comparing pooled gene lists of genes in module 1 to 4 of the scRNA-seq from Fig. 2 (upstream of Hmga1a) and genes in module 5 to 8 (downstream of Hmga1a) with genes significantly upregulated (**b**) or downregulated (**c**) in *hmga1a* OE CMs. (**d,e**) Venn diagrams comparing a list of previously identified[5] border zone genes with genes significantly upregulated (**d**) or downregulated (**e**) in *hmga1a* OE CMs.

https://doi.org/10.1038/s44161-024-00588-9

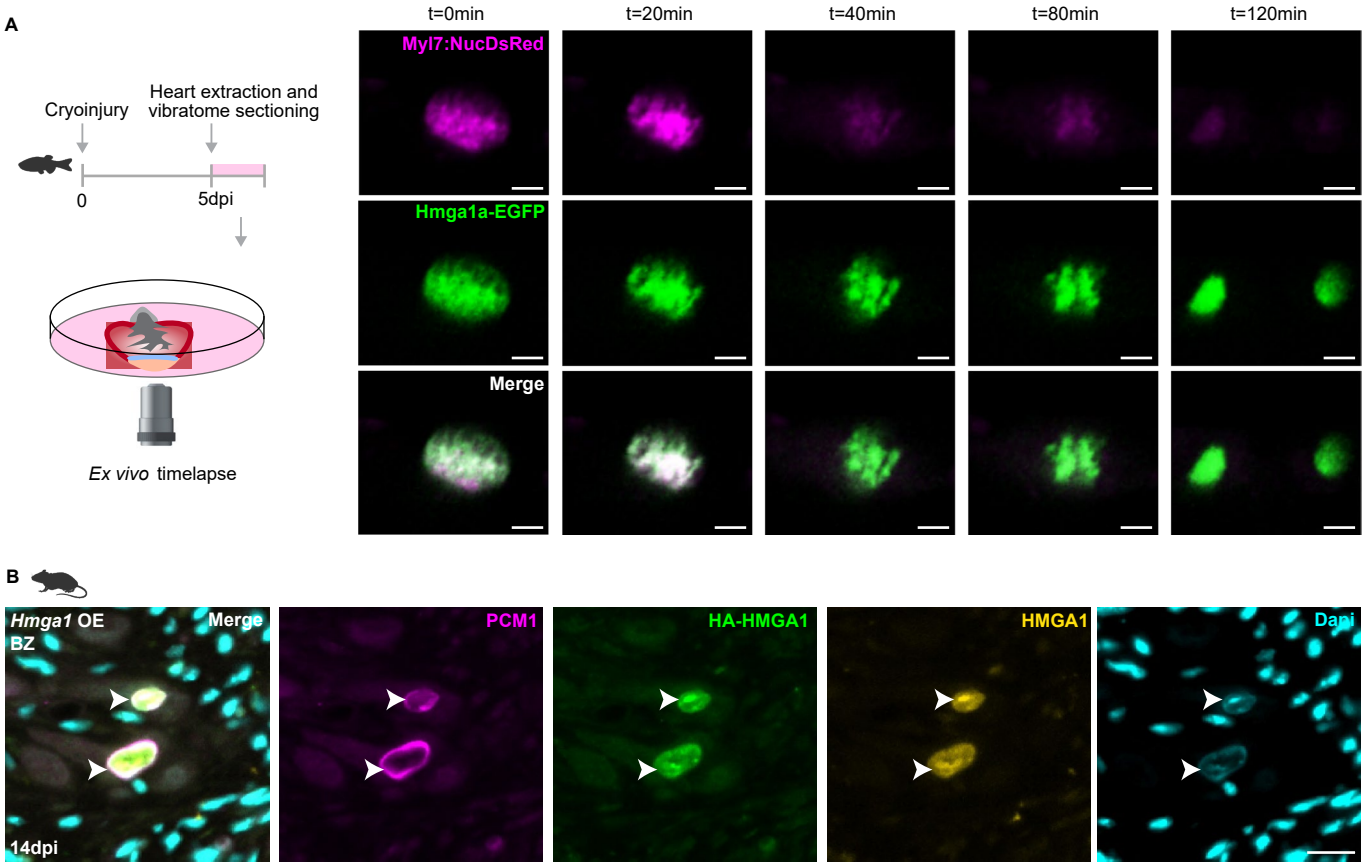

Extended Data Fig. 6 | Nuclear localization and chromatin binding of Hmga1 in zebrafish and mouse CMs. (**a**) *Ex vivo* time lapse imaging on vibratome sections from a zebrafish ventricle showing a dividing cardiomyocyte nucleus of a 14dpT *Tg(ubi:Loxp-stop-Loxp-hmga1a-eGFP, myl7:NucDsRed)* zebrafish. Note retention of Hmga1a-eGFP at the chromatin after nuclear envelope breakdown (t = 40). n = 1 heart was imaged. Scale bar represents 5µm. (**b**) Representative image of immunofluorescent staining against PCM-1, HA, Hmga1 and Dapi, showing a border zone zoom in of a 14dpi mouse heart transduced with *AAV9(CMV:HA-Hmga1)*. n = 4 hearts were analyzed. Arrowheads indicate colocalization of Dapi, HA and Hmga1 within nuclei. Scale bar represents 5µm.

https://doi.org/10.1038/s44161-024-00588-9

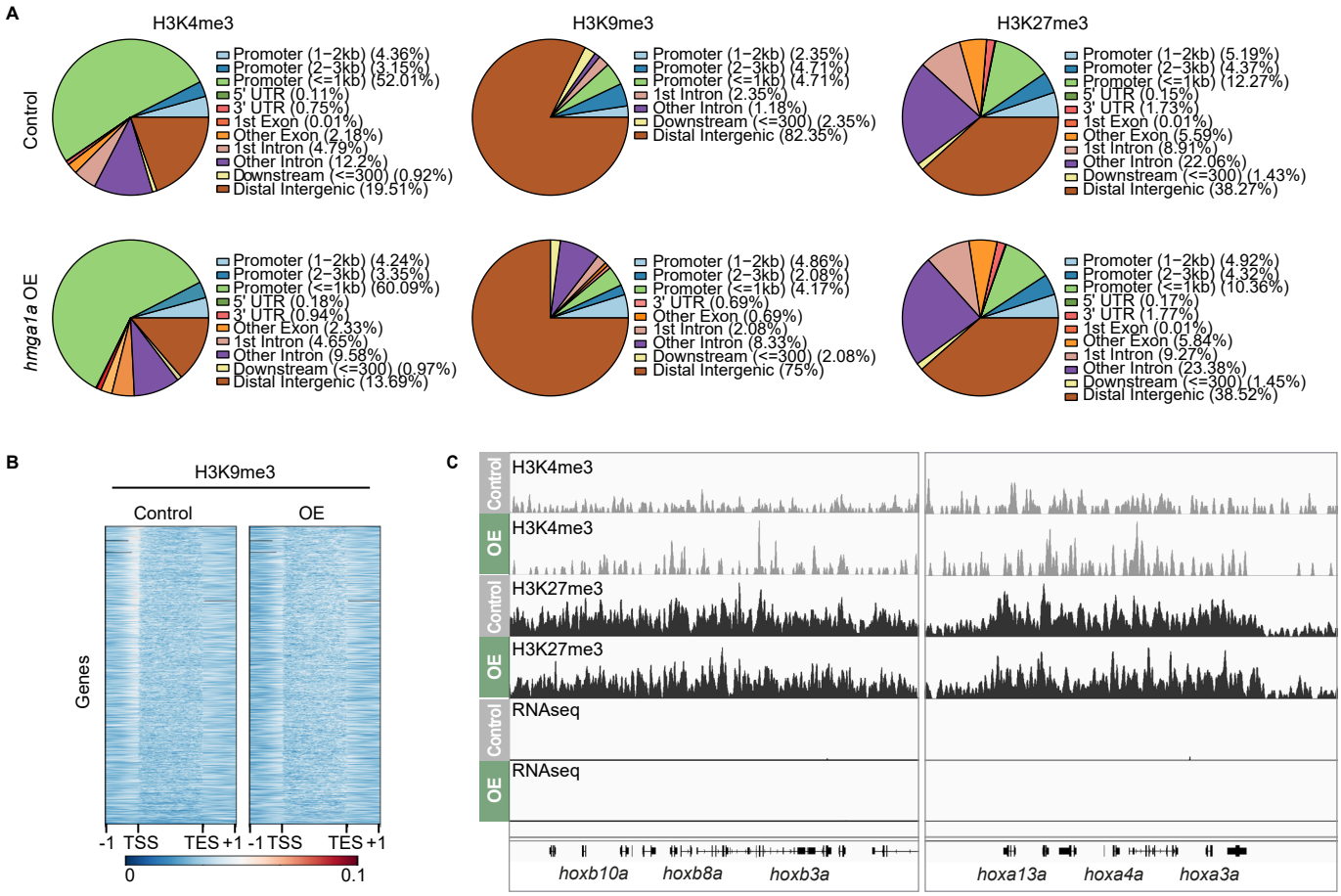

Extended Data Fig. 7 | ChICseq on zebrafish cardiomyocytes maps expected coverage of H3K4me3, H3K9me3 and H3K27me3 marks. (**a**) Pie charts showing percentages of genomic locations at which peaks are found in the sortChIC data for H3K4me3 marks, H3K9me3 marks and H3K27me3 marks in control and *hmga1a* OE CMs. H3K4me3 is enriched at promoter regions, while H3K9me3 and H3K27me3 are enriched on intergenic regions and gene bodies respectively. (**b**) Heatmap showing read distribution the levels of H3K9me3 in control and *hmga1a* OE CMs. (**c**) Zebrafish genome tracks showing hox cluster genes *hoxb10a, hoxb8a, hoxb3a, hoxa13a, hoxa4a* and *hoxa3a* that have no mRNA reads, no changes in H3K4me3 levels and no changes in H3K27me3 levels upon *hmga1a* OE.

https://doi.org/10.1038/s44161-024-00588-9

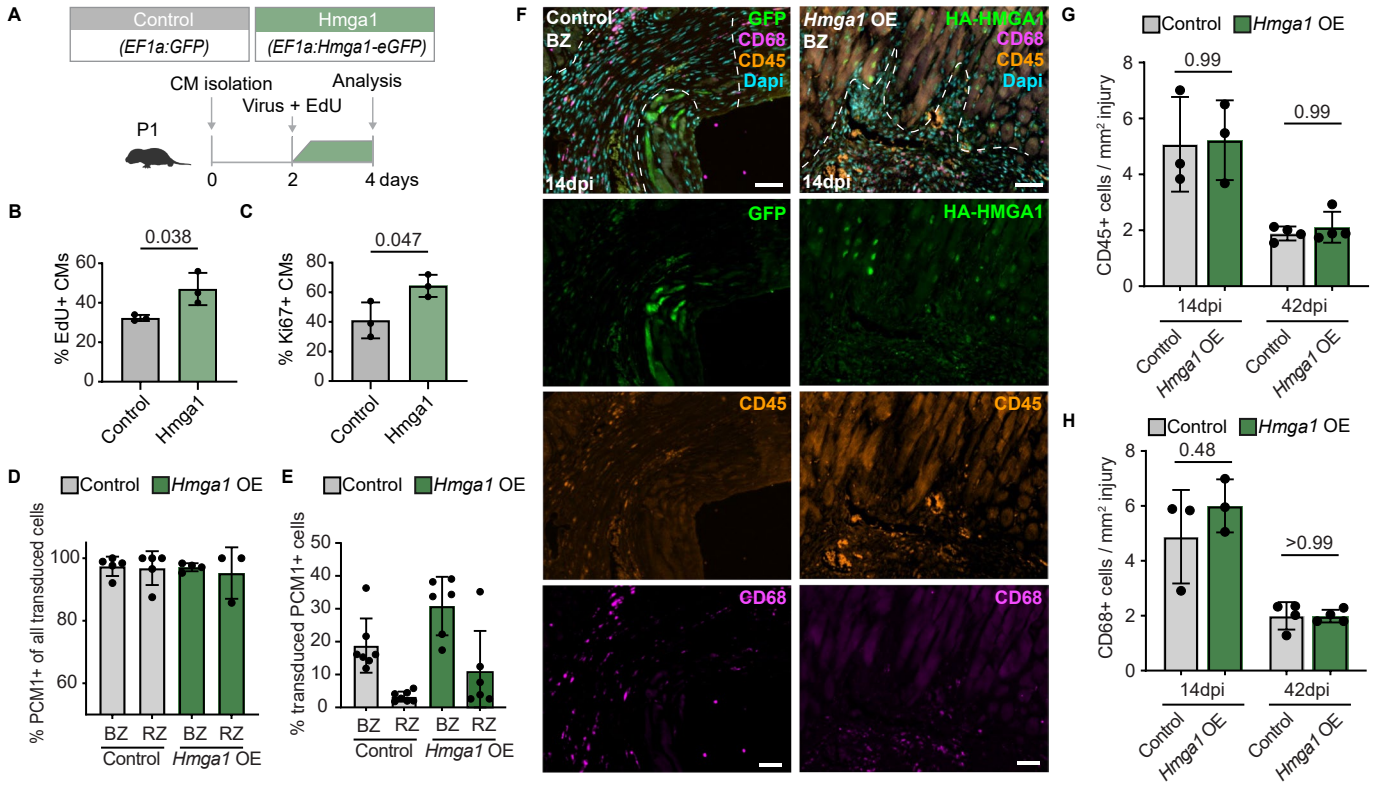

Extended Data Fig. 8 | Hmga1 stimulates cell cycle re-entry in neonatal rat cardiomyocytes and does not induce an aberrant inflammatory response in mouse. (**a**) Workflow of Hmga1-eGFP overexpression in neonatal rat cardiomyocytes (NRVMs) used in (**b-c**). (**b,c**) Quantification of EdU+ (**b**) and Ki67+ (**c**) cardiomyocytes in NRVMs transfected with *(EF1a:GFP)* (n = 3 biological replicates) or *EF1a:Hmga1-eGFP)* (n = 3 biological replicates). Datapoints represent individual samples. Error bars indicate mean ± SD. Statistics were performed using a two-tailed unpaired t-test and show a significant difference for % EdU+ CMs (p = 0.038), and for % Ki67+ CMs (p = 0.047). (**d**) Quantification of % of transduced cells that are PCM1 + , in the BZ and RZ of Control (n = 5) and *Hmga1* OE (n = 4) hearts. Datapoints represent individual hearts. Error bars indicate mean ± SD. (**e**) Quantification of cardiomyocyte transduction efficiency of Control (n = 7) and *Hmga1* OE (n = 6) virus in BZ and RZ. Datapoints represent individual hearts. Error bars indicate mean ± SD. (**f**) Representative images of immunofluorescent staining against GFP/HA-HMGA1, CD45, CD68 and Dapi, showing BZ zoom ins of 14dpi Control and *Hmga1* OE hearts. Dashed line indicates border between injury and CMs. Scale bars represent 30µm. (**g,h**) Quantifications of CD45+ (**g**) and CD68+ (**h**) cells per mm² injury area in 14dpi (n = 3 Control, n = 3 *Hmga1* OE) and 42dpi (n = 4 Control, n = 4 *Hmga1* OE) control and *Hmga1* OE hearts. Statistics were performed using a one-way ANOVA followed by Tukey's multiple comparisons test and show no significant differences between Control and *Hmga1* OE at 14dpi (p = 0.99) or 42dpi (p = 0.99) for CD45, and no significant differences between Control and *Hmga1* OE at 14dpi (p = 0.48) or 42dpi (p > 0.99) for CD68.

https://doi.org/10.1038/s44161-024-00588-9

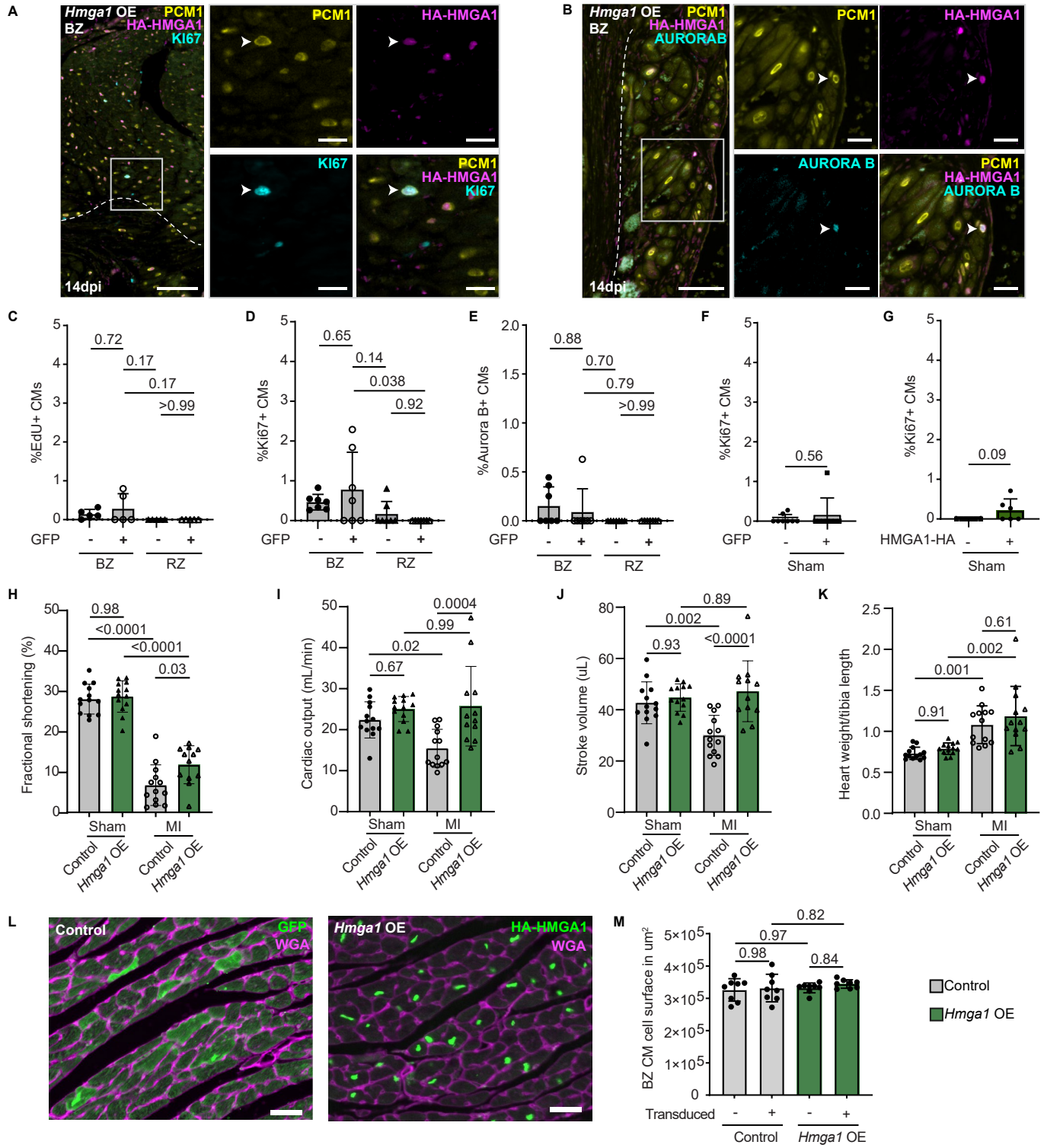

Extended Data Fig. 9 | See next page for caption.

https://doi.org/10.1038/s44161-024-00588-9

Extended Data Fig. 9 | *Hmga1* OE stimulates mammalian heart regeneration. (**a,b**) Representative image of immunofluorescent staining against PCM-1, HA and Ki67 (**a**) or Aurora B (**b**). Dashed line indicates injury border. Arrowheads indicate HMGA1-HA+ Ki67 + /Aurora B+ CMs. Scale bars represent 100µm in the overview and 20µm in the zoom ins. (**c-e**) Quantification of EdU+ (**c**), Ki67+ (**d**) and Aurora B+ (**e**) cardiomyocytes within the border zone (BZ) and remote zone (RZ) of Control hearts. n = 5 for EdU, n = 7 for Ki67 and n = 7 for Aurora B quantification. Datapoints represent individual hearts. Error bars indicate mean ± SD. Statistics were performed using a one-way ANOVA followed by Tukey's multiple comparisons test and show no significant differences except for %Ki67+ CMs comparing GFP + BZ CMs with GFP + RZ CMs (p = 0.038). (**f,g**) Quantifications of Ki67+ cardiomyocytes in Sham operated Control (n = 8) (**f**) and *Hmga1* OE (n = 6) (**g**) hearts. Datapoints represent individual hearts. Error bars indicate mean ± SD. Statistics were performed using a two-tailed unpaired t-test and show no significant difference in Control (p = 0.56) or *Hmga1* OE (p = 0.09) hearts. (**h-k**) Quantifications of 42dpi sham (n = 13 Control, n = 13 *Hmga1* OE) and MI (n = 13 Control, n = 12 *Hmga1* OE) hearts showing fractional shortening (**h**) (Control sham versus control MI p < 0.0001, Hmga1 OE sham versus Hmga1 OE MI p < 0.0001, control sham versus Hmga1 OE sham p = 0.98, control MI versus Hmga1 OE MI p = 0.03), cardiac output (**i**) (Control sham versus control MI p = 0.02, Hmga1 OE sham versus Hmga1 OE MI p = 0.99, control sham versus Hmga1 OE sham p = 0.67, control MI versus Hmga1 OE MI p = 0.0004), stroke volume (**j**) (Control sham versus control MI p = 0.002, Hmga1 OE sham versus Hmga1 OE MI p = 0.89, control sham versus Hmga1 OE sham p = 0.93, control MI versus Hmga1 OE MI p < 0.0001) and heart weight/tibia length (**k**) (Control sham versus control MI p = 0.001, Hmga1 OE sham versus Hmga1 OE MI p = 0.002, control sham versus Hmga1 OE sham p = 0.91, control MI versus Hmga1 OE MI p = 0.61). Datapoints represent individual hearts. Error bars indicate mean ± SD. Statistics were performed using a one-way ANOVA followed by Tukey's multiple comparisons test. (**l**) Representative image of immunofluorescent staining against GFP/HA-HMGA1 and WGA in uninjured mouse ventricles. Scale bars indicate 20µm. (**m**) Quantification of cell size based on WGA staining in (**l**), comparing Control (n = 8) versus *Hmga1* OE (n = 8) hearts, and untransduced CMs with transduced CMs. Datapoints represent individual hearts. Error bars indicate mean ± SD. Statistics were performed using a one-way ANOVA followed by Tukey's multiple comparisons test and show no significant differences between any of the conditions.

https://doi.org/10.1038/s44161-024-00588-9

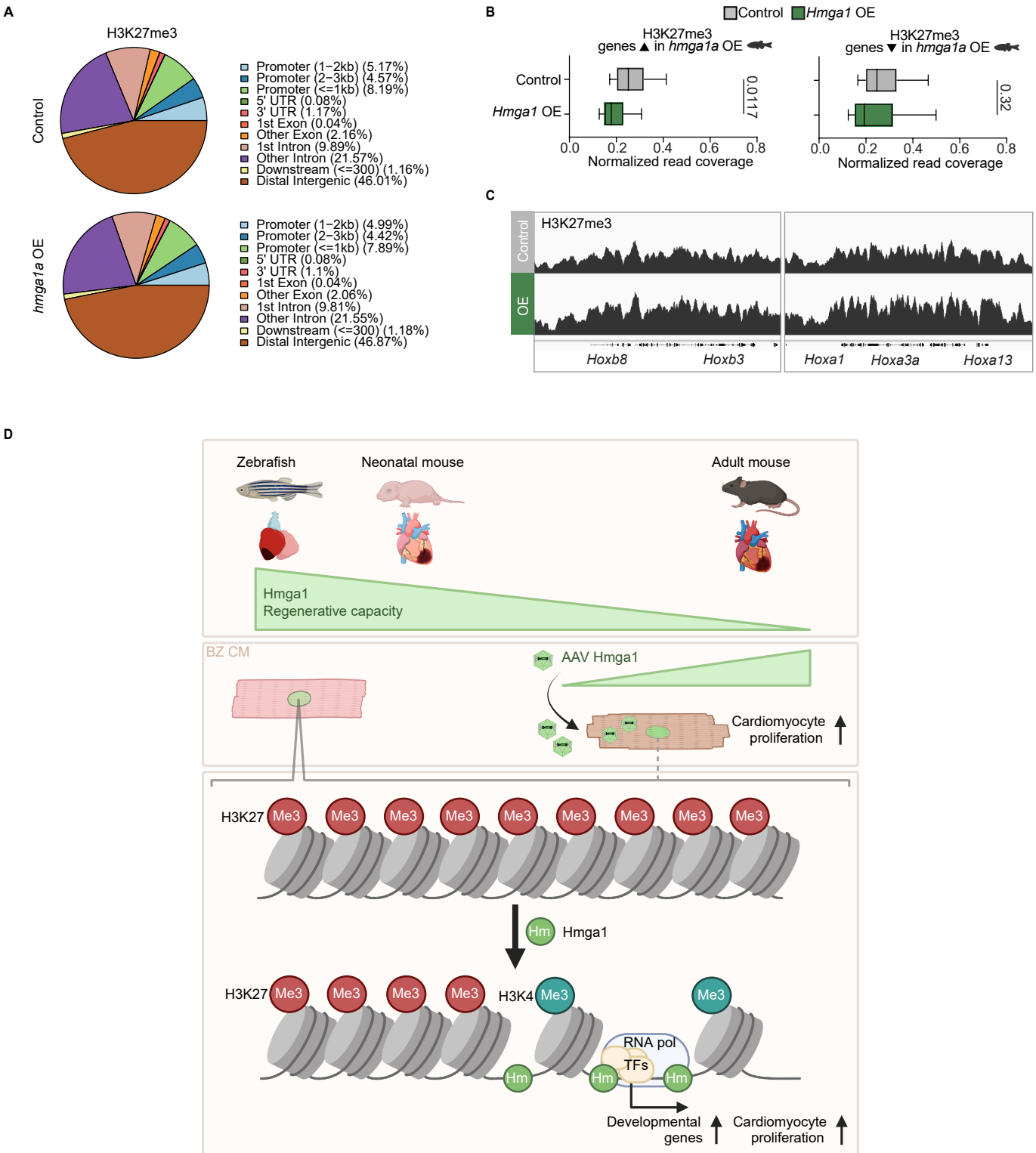

Extended Data Fig. 10 | *Hmga1* OE clears H3K27me3 levels in mouse BZ CMs. (**a**) Pie charts showing percentages of genomic locations at which peaks are found in the mouse sortChIC data for H3K27me3 marks in control and *Hmga1* OE CMs. H3K27me3 is enriched on intergenic regions and gene bodies respectively. (**b**) Quantification of H3K27me3 levels on orthologs of genes upregulated in *hmga1a* OE CMs (peak data on n = 1015 genes) and on genes downregulated in *hmga1a* OE CMs (peak data on n = 923 genes) in zebrafish, comparing normalized read coverage in Control versus *Hmga1* OE CMs. H3K27me3 levels are significantly reduced on gene bodies ($p < 0.001$) of orthologs of genes upregulated in *hmga1a* OE CMs, but not significantly different between control and *hmga1a* OE CMs on gene bodies of genes downregulated upon *hmga1a* OE. Centre line indicates median, whiskers indicate 10-90 percentile. Statistics were performed using two-tailed unpaired t-tests. (**c**) Mouse genome tracks showing hox cluster genes *Hoxb8, Hoxb3, Hoxa1, Hoxa3a and Hoxa13*. (**d**) Proposed model for the role of Hmga1 in regulating cardiomyocyte proliferation and cardiac regeneration. Created in BioRender. Bakkers, J. (2024) https://BioRender.com/v11t224.

nature portfolio

Corresponding author(s): Jeroen Bakkers

Last updated by author(s): Nov 16, 2024

Reporting Summary

Nature Portfolio wishes to improve the reproducibility of the work that we publish. This form provides structure for consistency and transparency in reporting. For further information on Nature Portfolio policies, see our Editorial Policies and the Editorial Policy Checklist.

Statistics

For all statistical analyses, confirm that the following items are present in the figure legend, table legend, main text, or Methods section.

n/a	Confirmed	
☐	☒	The exact sample size (*n*) for each experimental group/condition, given as a discrete number and unit of measurement
☐	☒	A statement on whether measurements were taken from distinct samples or whether the same sample was measured repeatedly
☐	☒	The statistical test(s) used AND whether they are one- or two-sided *Only common tests should be described solely by name; describe more complex techniques in the Methods section.*
☒	☐	A description of all covariates tested
☐	☒	A description of any assumptions or corrections, such as tests of normality and adjustment for multiple comparisons
☐	☒	A full description of the statistical parameters including central tendency (e.g. means) or other basic estimates (e.g. regression coefficient) AND variation (e.g. standard deviation) or associated estimates of uncertainty (e.g. confidence intervals)
☐	☒	For null hypothesis testing, the test statistic (e.g. *F*, *t*, *r*) with confidence intervals, effect sizes, degrees of freedom and *P* value noted *Give P values as exact values whenever suitable.*
☒	☐	For Bayesian analysis, information on the choice of priors and Markov chain Monte Carlo settings
☒	☐	For hierarchical and complex designs, identification of the appropriate level for tests and full reporting of outcomes
☐	☒	Estimates of effect sizes (e.g. Cohen's *d*, Pearson's *r*), indicating how they were calculated

Our web collection on statistics for biologists contains articles on many of the points above.

Software and code

Policy information about availability of computer code

Data collection	Leica Application Suite (LAS X, version 3.30 or newer) was used for image aquisition of confocal microscopy data. Chemiluminescence on wetsren blots was recorded using the ImageQuant software v7.1 of the ImageQuant LAS Imaging system (GE Healthcare)
Data analysis	Galaxy (usegalaxy.org) versions v22.05 through v24.1 were used to analyse ChICseq data. The Database for Annotation, Visualization and Integrated Discovery (DAVID) was used for Gene Ontology analyses. Statistics were performed in Graphpad Prism software V9.5.0. Vevo lab version 5.7.1 was used for echocardiography analysis Histological analysis and quantifications were performed using Imaris x64 V3.2.1 software and ImageJ version 1.53c

For manuscripts utilizing custom algorithms or software that are central to the research but not yet described in published literature, software must be made available to editors and reviewers. We strongly encourage code deposition in a community repository (e.g. GitHub). See the Nature Portfolio guidelines for submitting code & software for further information.

Data

Policy information about availability of data

All manuscripts must include a data availability statement. This statement should provide the following information, where applicable:

- Accession codes, unique identifiers, or web links for publicly available datasets
- A description of any restrictions on data availability
- For clinical datasets or third party data, please ensure that the statement adheres to our policy

All sequencing data can be found on GEO in record GSE241159. Mouse TOMO-seq data can also be viewed and searched at http://mouse.genomes.nl/tomoseq/2018/

Research involving human participants, their data, or biological material

Policy information about studies with human participants or human data. See also policy information about sex, gender (identity/presentation), and sexual orientation and race, ethnicity and racism.

Reporting on sex and gender	Age and gender was not collected
Reporting on race, ethnicity, or other socially relevant groupings	*Please specify the socially constructed or socially relevant categorization variable(s) used in your manuscript and explain why they were used. Please note that such variables should not be used as proxies for other socially constructed/relevant variables (for example, race or ethnicity should not be used as a proxy for socioeconomic status).* *Provide clear definitions of the relevant terms used, how they were provided (by the participants/respondents, the researchers, or third parties), and the method(s) used to classify people into the different categories (e.g. self-report, census or administrative data, social media data, etc.)* *Please provide details about how you controlled for confounding variables in your analyses.*
Population characteristics	Age and gender was not collected
Recruitment	N/A
Ethics oversight	Paraffin-embedded infarcted human heart tissue was handled in a coded manner that met the criteria of the Code of Conduct used in the Netherlands for the responsible use of human tissue in medical research (www.federa.org/codes-conduct). Collection of the archive material was approved by the biobank review committee (protocol 15–252) from the University Medical Center Utrecht.

Note that full information on the approval of the study protocol must also be provided in the manuscript.

Field-specific reporting

Please select the one below that is the best fit for your research. If you are not sure, read the appropriate sections before making your selection.

☒ Life sciences ☐ Behavioural & social sciences ☐ Ecological, evolutionary & environmental sciences

For a reference copy of the document with all sections, see nature.com/documents/nr-reporting-summary-flat.pdf

Life sciences study design

All studies must disclose on these points even when the disclosure is negative.

Sample size	Sample size was determined using power analyses and based on previous experiments conducted in the lab
Data exclusions	no data was excluded
Replication	When possible, experiments were conducted at least twice independently. All attempts at replication were successful
Randomization	Mice were allocated randomly into groups. Wildtype zebrafish were allocated randomly into groups. Zebrafish were allocated into groups based on their genetic background when applicable (mutant versus siblings, control construct versus overexpression).
Blinding	Quantifications were performed in a blinded fashion.

Reporting for specific materials, systems and methods

We require information from authors about some types of materials, experimental systems and methods used in many studies. Here, indicate whether each material, system or method listed is relevant to your study. If you are not sure if a list item applies to your research, read the appropriate section before selecting a response.

Materials & experimental systems

n/a	Involved in the study
☐	☒ Antibodies
☐	☒ Eukaryotic cell lines
☒	☐ Palaeontology and archaeology
☐	☒ Animals and other organisms
☒	☐ Clinical data
☒	☐ Dual use research of concern
☒	☐ Plants

Methods

n/a	Involved in the study
☒	☐ ChIP-seq
☒	☐ Flow cytometry
☒	☐ MRI-based neuroimaging

Antibodies

Antibodies used

anti-PCNA (Dako #M0879, 1:800), anti-GFP (aves #GFP-1010, 1:1000), anti-Mef2c (Santa Cruz #SC313, Biorbyt #orb256682 both 1:1000), anti-phosphor-S6 ribosomal protein (ser235/236) (Cell Signaling Technology #4858 1:500), anti-Tri-Methyl-Histone H3 (Lys27)(C36B11)(Cell Signaling Technology #9733T 1:300), anti-α-actinin (Sigma #A7811 1:500), anti-Tropomyosin (Sigma #T9283 1:500), anti-HA (Abcam #ab9111 or BioLegend #901501 both 1:200), anti- PCM (Atlas #HPA023370 1:400), anti-Tri-Methyl-Histone H3 (Lys27) (C36B11) (Cell Signaling Technology #9733T 1:300), anti-Ki-67 (SolA15) (eBioscience Invitrogen #15227437 1:1000), anti-Aurora-B (AIM1) (BD Biosciences #611082 1:300), H3K4me3 (Invitrogen #MA-5-11199, 1:400), H3K9me3 (Invitrogen, MA5-33395, 1:200), H3K27me3 (Cellsignal #C36B11, 1:200), anti-HMGA1 (Abcam AB129153, 1:1000), anti-a-tubulin (Calbiochem CP06-100UG 1:1000), Anti-Mouse CD45 (BD biosciences #553076, 1:200), Anti-Rabbit CD68 (Abcam #ab125212, 1:200).

anti-chicken Alexa488 (Thermofisher, #A11039, 1:500), anti-mouse Alexa488 (Thermofisher, #A21133, 1:500), anti-rabbit Alexa555 (Thermofisher, #A21428, 1:500), anti-mouse Alexa555 (Thermofisher, #A21127, 1:500), anti-mouse Alexa633 (Thermofisher, #A21050, 1:500), anti-mouse Cy5 (Jackson ImmunoR, #118090, 1:500)

Validation

all antibodies have been used in publications and have validations detailed on the company website
Anti-PCNA (Dako #M0879, 1:800)
https://www.agilent.com/store/en_US/Prod-M087901-2/M087901-2

Anti-GFP (Aves Labs #GFP-1010, 1:1000)
https://www.antibodiesinc.com/products/anti-green-fluorescent-protein-antibody-gfp

Anti-Mef2c (Santa Cruz #SC313, 1:1000)
https://www.scbt.com/p/mef2c-antibody-c-21

Anti-Mef2c (Biorbyt #orb256682, 1:1000)
https://www.biorbyt.com/mef2c-antibody-orb256682.html

Anti-phospho-S6 Ribosomal Protein (Ser235/236) (Cell Signaling Technology #4858, 1:500)
https://www.cellsignal.com/products/primary-antibodies/phospho-s6-ribosomal-protein-ser235-236-antibody/4858

Anti-Tri-Methyl-Histone H3 (Lys27) (C36B11) (Cell Signaling Technology #9733T, 1:300)
https://www.cellsignal.com/products/primary-antibodies/tri-methyl-histone-h3-lys27-antibody-c36b11/9733

Anti-α-Actinin (Sigma #A7811, 1:500)
https://www.sigmaaldrich.com/catalog/product/sigma/a7811

Anti-Tropomyosin (Sigma #T9283, 1:500)
https://www.sigmaaldrich.com/catalog/product/sigma/t9283

Anti-HA (Abcam #ab9111, 1:200)
https://www.abcam.com/ha-tag-antibody-16b12-ab9111.html

Anti-HA (BioLegend #901501, 1:200)
https://www.biolegend.com/en-us/products/anti-ha-tag-antibody-901501

Anti-PCM (Atlas Antibodies #HPA023370, 1:400)
https://www.atlasantibodies.com/products/primary-antibodies/anti-pcm1-antibody-hpa023370

Anti-Ki-67 (SolA15) (eBioscience Invitrogen #15227437, 1:1000)
https://www.thermofisher.com/antibody/product/Ki-67-Antibody-clone-SolA15-Monoclonal/14-5698-82

Anti-Aurora-B (AIM1) (BD Biosciences #611082, 1:300)
https://www.bdbiosciences.com/en-us/products/reagents/research-reagents/antibodies/anti-aurora-b-aim-1.611082

Anti-H3K4me3 (Invitrogen #MA5-11199, 1:400)
https://www.thermofisher.com/antibody/product/H3K4me3-Antibody-MA5-11199

H3K9me3 (Invitrogen, MA5-33395, 1:200)
https://www.thermofisher.com/antibody/product/H3K9me3-Antibody-MA5-33395

H3K27me3 (Cell Signaling Technology #C36B11, 1:200)
https://www.cellsignal.com/products/primary-antibodies/tri-methyl-histone-h3-lys27-antibody-c36b11/9733

Anti-HMGA1 (Abcam AB129153, 1:1000)
https://www.abcam.com/hmga1-antibody-ab129153.html

Anti-α-Tubulin (Calbiochem CP06-100UG, 1:1000)
https://www.merckmillipore.com/CP06-100UG

Anti-Mouse CD45 (BD Biosciences #553076, 1:200)
https://www.bdbiosciences.com/en-us/products/reagents/research-reagents/antibodies/anti-mouse-cd45.553076

Anti-Rabbit CD68 (Abcam #ab125212, 1:200)
https://www.abcam.com/cd68-antibody-ab125212.html

Anti-Chicken Alexa488 (Thermo Fisher #A11039, 1:500)
https://www.thermofisher.com/antibody/product/Alexa-Fluor-488-Antibody-Polyclonal/A-11039

Anti-Mouse Alexa488 (Thermo Fisher #A21133, 1:500)
https://www.thermofisher.com/antibody/product/Alexa-Fluor-488-Antibody-Polyclonal/A-21133

Anti-Rabbit Alexa555 (Thermo Fisher #A21428, 1:500)
https://www.thermofisher.com/antibody/product/Alexa-Fluor-555-Antibody-Polyclonal/A-21428

Anti-Mouse Alexa555 (Thermo Fisher #A21127, 1:500)
https://www.thermofisher.com/antibody/product/Alexa-Fluor-555-Antibody-Polyclonal/A-21127

Anti-Mouse Alexa633 (Thermo Fisher #A21050, 1:500)
https://www.thermofisher.com/antibody/product/Alexa-Fluor-633-Antibody-Polyclonal/A-21050

Anti-Mouse Cy5 (Jackson ImmunoResearch #118090, 1:500)
https://www.jacksonimmuno.com/catalog/product/118-090-003

Eukaryotic cell lines

Policy information about cell lines and Sex and Gender in Research

Cell line source(s)	HEK-293 cells were bought from ATCC
Authentication	None of the cell lines were authenticated
Mycoplasma contamination	all cell lines tested negative for mycoplasm
Commonly misidentified lines (See ICLAC register)	no commonly misidentified cell lines were used

Animals and other research organisms

Policy information about studies involving animals; ARRIVE guidelines recommended for reporting animal research, and Sex and Gender in Research

Laboratory animals	mouse experiments: Mus musculus, C57bl/6, between 7-12 weeks of age Mice were housed under normal conditions with food and water ad libitum under normal day and night cycles in monitored environmental conditions. zebrafish experiments: Danio Rerio, Tupfel Long-Fin (TL), between 6-18 months of age
Wild animals	Study did not involve wild animals.
Reporting on sex	For mouse experiments, only male animals were used. Literature strongly suggests that sex difference can be an independent factor in studies related to cardiac biology (Pham et al.). Studies in mice, rats and human patients have shown that it has a significant influence on heart function and the cause, clinical manifestation and prognosis of heart disease. Specifically, in a mouse model of myocardial infarction injury, myocardial injury is reduced in female compared to male hearts, and this reduction is dependent on estrogen-signalling. Due to these differences in cardiac biology between males and females, we use males only in this experiment. For zebrafish experiments, males and females were used in all experiments.
Field-collected samples	Study did not include field-collected samples

Ethics oversight	All procedures involving animals were approved by the local animal experiments committees at the Hubrecht Institute-KNAW and at the Amsterdam University Medical Centers and performed in compliance with animal welfare laws, guidelines, and policies, according to national and European law.

Note that full information on the approval of the study protocol must also be provided in the manuscript.